Synthesis and characterization of Mo-B based protective coatings

Von der Fakultät für Georessourcen und Materialtechnik der Rheinisch -Westfälischen Technischen Hochschule Aachen

zur Erlangung des akademischen Grades eines

Doktors der Ingenieurwissenschaften

genehmigte Dissertation

vorgelegt von

Jan-Ole Achenbach, M. Sc.

aus Oldenburg

Berichter: Herr Univ.-Prof. Jochen M. Schneider, Ph.D.
Herr Univ.-Prof. Dipl.-Ing. Dr. mont. Paul H. Mayrhofer

Tag der mündlichen Prüfung: 24.06.2020

Diese Dissertation ist auf den Internetseiten der Universitätsbibliothek online verfügbar

Materials Chemistry Dissertation

No.: 33 (2020)

Jan-Ole Achenbach

Synthesis and characterization of Mo-B based protective coatings



Abstract

In the first part of this thesis, the angle-resolved composition evolution of Mo-B-C thin films deposited from a Mo₂BC compound target is investigated experimentally and theoretically. Depositions were carried out by direct current magnetron sputtering (DCMS) in a pressure range from 0.09 to 0.98 Pa in Ar and Kr. The substrates were placed at specific angles α with respect to the target normal from 0 to ± 67.5°. A model based on TRIDYN and SIMTRA was used to calculate the influence of the sputtering gas on the angular distribution function of the sputtered species at the target, their transport through the gas phase and film composition. Experimental pressure and sputtering gas dependent thin film chemical composition data were in good agreement with simulated angle-resolved film composition data. In Ar, the pressure-induced film composition variations at a particular a were within the error of the EDX measurements. Contrary, an order of magnitude increase in Kr pressure resulted in an increase of the Mo concentration measured at $\alpha = 0^{\circ}$ from 36 to 43 at. %. It is shown that the mass ratio between sputtering gas and sputtered species defines the scattering angle within the collision cascades in the target, as well as for the collisions in the gas phase, which in turn define the angle- and pressure-dependent film compositions. In the second part, the low temperature oxidation behavior of crystalline Mo₂BC thin films was systematically investigated. Mo₂BC exhibits a unique combination of high stiffness and moderate ductility, enabling the application as protective and wear resistant coating. As the low temperature oxidation behavior of Mo₂BC coatings is unexplored, direct current magnetron sputtered Mo₂BC coatings were oxidized at temperatures ranging from 500 to 100°C for up to 28 days. Time-of-Flight elastic recoil detection analysis reveals that the onset of oxidation takes place at approximately 300°C as a significant increase in the O content was observed. Crystalline

oxide scales containing orthorhombic MoO₃ were identified after oxidation for 15 min at 500°C and 10 days at 200°C. Isothermal oxidation at 200 and 100°C exhibit oxide scale thicknesses of 401 nm ± 33 nm and 22 nm ± 10 nm after 14 days. Oxidation for 28 days at 100 °C exhibits an oxide scale thickness of 13 nm ± 3 nm which is comparable to the aforementioned oxide scale thickness after oxidation for 14 days at 100°C. Based on the combination of mechanical properties and the here reported low temperature oxidation behavior Mo₂BC coatings qualify for application in solid wood machining and low temperature forming processes at temperatures close to 100°C or below. In the third and last part of this thesis, the first thin film synthesis of MoAlB coatings is communicated. MoAIB was reported to be the only oxidation resistant transition metal boride as it forms a dense, adherent alumina scale. While, based on X-ray diffraction investigations, the formation of phase pure orthorhombic MoAIB coatings was observed, energy dispersive X-ray spectroscopy carried out in a scanning transmission electron microscope revealed the presence of Al-rich and O-rich regions within the MoAlB matrix. The oxidation kinetics of coatings and bulk was comparable as the scale thickness formed on the MoAIB coating after oxidation at 1200°C for 30 minutes was similar to the one extrapolated for bulk MoAlB. Furthermore, the oxidation kinetics of MoAlB coatings was significantly lower as the one reported for bulk Ti₂AlC. Finally, the elastic properties measured for the as deposited coatings were consistent with ab initio predictions.

Zusammenfassung

Der erste Teil dieser Arbeit beschäftigt sich mit der experimentellen und theoretischen Untersuchung der winkelabhängigen Zusammensetzungsentwicklung von Mo₂BC Dünnschichten synthetisiert von einem Mo₂BC Komposit-Target. Die Beschichtungen wurden mittels Gleichstrommagnetronsputtern sowohl in Ar als auch in Kr in einem Druckbereich von 0.09 bis 0.98 Pa durchgeführt. Während der Beschichtungen wurden die Proben im spezifischen Winkelbereichen α von 0 bis ±67.5° hinsichtlich der Targetnormalen ausgerichtet. Ein auf TRIDYN und SIMTRA basierendes Modell wurde verwendet, um den Einfluss des Sputtergases auf die Winkelverteilungsfunktion der gesputterten Spezies am Target, deren Transport durch die Gasphase, sowie die chemische Zusammensetzung am Substrat zu berechnen. Experimentelle und simulierte druck- und sputtergasabhängige Dünnschichtzusammensetzungen zeigten eine gute Übereinstimmung. Bei der Verwendung von Ar lagen die druckinduzierten Änderungen der Zusammensetzung bei einzelnen α innerhalb der EDX Messgenauigkeit. Hingegen führte eine Kr Druckerhöhung von einer Größenordnung zu einem Anstieg im Mo Gehalt bei $\alpha = 0^{\circ}$ von 36 zu 43 at. %. Es wurde gezeigt, dass das Masseverhältnis vom Sputtergas und gesputterten Spezies nicht nur die Streuung innerhalb der Kollisionskaskaden im Target, sondern auch die Streuung durch Gasphasenkollision und somit letztendlich die winkel- und druckabhängige Schichtzusammensetzung definiert. Im zweiten Teil wird das Niedertemperatur-Oxidationsverhalten von kristallinen Mo₂BC Dünnschichten systematisch untersucht. Mo₂BC zeichnet sich durch eine einzigartige Kombination von hoher Steifigkeit und moderater Duktilität aus, welche die Verschleißschutzschicht Verwendungen Mo₂BC ermöglicht. von als Das Oxidationsverhalten von Mo₂BC bei geringen Temperaturen wurde noch nicht erforscht. Deshalb wurden gleichstrommagnetrongesputterte Mo₂BC Schichten in einem Temperaturbereich von 500 bis 100°C für bis zu 28 Tage oxidiert. Elastische Rückstreudetektionsanalyse zeigte den Beginn der Oxidation bei ungefähr 300°C, welche durch einen signifikanten Anstieg im Sauerstoffgehalt festgestellt werden konnte. Kristalline Oxidschichten, die orthorhombisches MoO₃ beinhalten, wurden erstmals nach Oxidation für 15 min bei 500°C und nach 10 Tagen bei 200°C beobachtet. Isotherme Oxidation für 14 Tage bei 200 und 100°C resultierten in Oxidschichtdicken von 401 nm ± 33 nm und 22 nm ± 10 nm. Die Probe oxidiert für 28 Tage bei 100°C zeigt eine Oxidschichtdicke von 13 nm ± 3 nm welche vergleichbar zur vorher genannten Oxidschichtdicke nach Oxidation für 14 Tage bei 100°C ist. Die Kombination aus mechanischen Eigenschaften mit dem hier untersuchten Oxidationsverhalten bei niedrigen Temperaturen qualifiziert Mo₂BC Schichten für eine Anwendung in der Massivholzbearbeitung und in Niedrigtemperatur-Umformprozessen bei Temperaturen nahe 100°C oder niedriger. Im dritten und letzten Teil dieser Arbeit wird die erste Dünnschichtensynthese von MoAIB kommuniziert. Über MoAIB wurde berichtet, dass es das einzige oxidationsresistente Übergangsmetall-Borid ist, da es eine dichte und adhärente Aluminiumoxidschicht bildet. Mittels Röntgenbeugung wurde die Bildung von MoAIB Energiedispersive phasenreinem beobachtet. Röntgenspektroskopie, durchgeführt in einem Transmissions-elektronenmikroskop, zeigte sowohl Al- als auch Oreiche Regionen in der MoAlB Matrix. Der Vergleich der gebildeten Oxidschichtdicke auf MoAlB Dünnschichten mit extrapolierten Werten für Bulkproben zeigte, dass das Oxidationsverhalten von Dünnschichten und Bulkproben vergleichbar ist. Weiterhin wiesen MoAIB Dünnschichten eine signifikant geringere Oxidationskinetik im Vergleich zu Ti₂AlC Bulkproben auf. Zusätzlich stimmten die gemessenen elastischen Eigenschaften von MoAIB mit den ab initio Vorhersagen überein.

Preface

This work was supported by the German Science Foundation (DFG) under project number DFG SCHN 735/35-1. DFT calculations were performed with computing resources granted by JARA-HPC from RWTH Aachen University under project no. JARA0131. Furthermore, financial support for the operation of the accelerator laboratory in Uppsala by VR-RFI (contract #821-2012-5144 and #2017-00646_9) and the Swedish Foundation for Strategic Research (SSF, contract RIF14-0053) is gratefully acknowledged.

The following papers contributed to this thesis:

Paper I

Achenbach, J.-O., Mráz, S., Primetzhofer, D., & Schneider, J.M. Correlative Experimental and Theoretical Investigation of the Angle-Resolved Composition Evolution of Thin Films Sputtered from a Compound Mo₂BC Target. Coatings 2019, 9(3), 206.

Paper II

Achenbach, J.-O., Karimi Aghda, S., Hans, M., Primetzhofer, D., Holzapfel, D.M., Miljanovic D.J., & Schneider, J.M. Low temperature oxidation behavior of Mo₂BC coatings. Accepted for publication JVSTA

Paper III

Achenbach, J.-O.; Sahu, R.; Völker, B.; Hans, M.; Primetzhofer, D.; Miljanovic, D.J.; Scheu, C.; Schneider, J.M. Synthesis and Properties of Orthorhombic MoAIB Coatings. Coatings 2019, 9, 510.

Contribution to the papers

All research questions and scientific strategies were conceived by JOA together with JMS.

The first draft of all manuscripts was compiled by JOA. All co-authors contributed in the evaluation and discussion of results as well as in editing the papers.

Paper I – Coating synthesis was carried out by JOA with the help of SM. Chemical composition was analyzed by JOA with reference samples measured by DP. Structural characterization was done by JOA. *Ab initio* calculations were conducted by JOA. Monte Carlo simulations were done by JOA with the help of SM.

Paper II – Coating synthesis and oxidation experiments was carried out by JOA with the help of DJM. TiN interlayer was deposited by DMH. FIB Lamellae preparation, STEM analysis and EDX lines scans were carried out by SKA. ERDA was performed by MH and DP. Structural characterization was done by JOA with the help of DJM.

Paper III – Coating synthesis and oxidation was carried out by JOA with the help of DJM. Chemical composition was analyzed by JOA with the help of DJM with a reference sample measured by DP and MH. Structural characterization was done by JOA with the help of DJM. Nanoindentation was performed by JOA with the help of DJM. High resolution transmission electron microscopy, selected area electron diffraction, and electron energy loss spectroscopy were done by RS, BV and CS. Principle compound analysis of EDX

maps was performed by RS, BV and CS. Scanning electron microscopy of the oxidized samples was performed by BV and MH.

Publications related to the topics of the thesis

Paper IV

Nanostructure of and structural defects in a Mo₂BC hard coating investigated by transmission electron microscopy and atom probe tomography

Stephan Gleich, Hanna Fager, Hamid Bolvardi, Jan-Ole Achenbach, Rafael Soler, Konda Gokuldoss Pradeep, Jochen M. Schneider, Gerhard Dehm, and Christina Scheu Journal of Applied Physics **122**, 075305 (2017)

Paper V

Modifying the nanostructure and the mechanical properties of Mo₂BC hard coatings: Influence of substrate temperature during magnetron sputtering

Stephan Gleich, Rafael Soler, Hanna Fager, Hamid Bolvardi, Jan-Ole Achenbach, Marcus Hans, Daniel Primetzhofer, Jochen M. Schneider, Gerhard Dehm, Christina Scheu

Materials and Design 142 (2018) 203-211

Other publications:

Paper VII

Guiding ab initio calculations by alchemical derivatives

Moritz to Baben, Jan-Ole Achenbach, and O. Anatole von Lilienfeld

The Journal of Chemical Physics **144**, 104103 (2016); doi: 10.1063/1.4943372

Paper VIII

Correlative theoretical and experimental investigation of the formation of AIYB14 and competing phases

Oliver Hunold, Yen-Ting Chen, Denis Music, Per O. Å. Persson, Daniel Primetzhofer, Moritz to Baben, Jan-Ole Achenbach, Philipp Keuter, and Jochen M. Schneider Journal of Applied Physics **119**, 085307 (2016); doi: 10.1063/1.4942664

Danksagung:

Als erstes richtet sich meine Dankbarkeit an meinen Betreuer und Doktorvater Prof. Jochen M. Schneider. Ich danke dir für die letzten 7 Jahre, in denen ich als Hiwi und schließlich als Doktorand am Lehrstuhl für Werkstoffchemie arbeiten durfte. Ganz besonders danke ich dir für deine begeisternde und erleuchtende Präsentation am Tag der Ingenieurswissenschaften 2010, welche mich überhaupt erst motiviert hat das Werkstoffingenieurwesen zu studieren. Du strahlst stets eine Kompetenz aus, die Menschen in deinem Umfeld mitreißt und zu Höchstleistungen motiviert. In den letzten 4 Jahren gab es genug Tage an denen ich mit wenig Zuversicht über neue Daten in dein Büro spazierte, es aber wieder mit voller Zuversicht verließ.

Jochen, vielen Dank für deine Geduld und alles was du mir beigebracht hast!

Als zweites richtet sich mein Dank an meinen Zweitgutachter Prof. Paul Mayrhofer. Vielen Dank für die kompetenten und aufschlussreichen Diskussionen während unserer Workshops in Wien und Aachen. Dieser Dank richtet sich gleichermaßen an alle Mitarbeiter deiner Gruppe.

Auch möchte ich mich bei Moritz und Stano bedanken. Ich hatte das Privileg euer Hiwi sein zu dürfen und wurde während dieser Zeit ideal auf die damals noch bevorstehende Doktorandenzeit vorbereitet. Ohne eure ausführliche Einweisung in die DFT sowie das korrekte experimentelle Arbeiten wäre diese Arbeit nicht möglich gewesen. Eure Fachliche (theoretisch wie experimentelle) Kompetenz sucht ihres gleichen.

Mein nächster ganz besonderer Dank richtet sich an meinen "Office Buddy" der letzten 4 Jahre. Philipp, für dich kann ich meinen Dank nicht weiter spezifizieren da er so gut wie jeden Aspekt meiner Doktorandenzeit betrifft. Ob es sich um DFT, Synthese, Analyse, Daten Interpretation, Schreiben, Lehre oder welches arbeitsrelevante Thema auch immer handelt, du konntest mir steht konstruktiv zur Seite stehen. All unsere Diskussionen werden mir fehlen. Ich freue mich in dir einen Freund gefunden zu haben.

Ich danke allen weiteren Kollegen des MCh's, den wissenschaftlichen sowie auch den nicht wissenschaftlichen. Ich hoffe es nimmt mir keiner Übel, wenn ich nicht jeden Namen einzeln aufzähle. Danke für eure Unterstützung, eurer Hilfsbereitschaft und dem jederzeit äußerst angenehmen Arbeitsklima.

Ich danke meinen Freunden für die notwendige Ablenkung außerhalb der Arbeitszeit. Ganz besonders danke ich Roland, Michi und Fabrice für die spannenden interdisziplinären Diskussionsrunden bei einem gemütlichen Bier.

Ebenfalls bin ich meiner Familie überaus Dankbar. Ihr habt mich jederzeit unterstützt, motiviert und mir das Studium überhaupt erst ermöglicht.

Zuletzt geht mein Dank an meine zukünftige Frau Jenny. Danke für deine Unterstützung, deine Geduld und das du immer für mich da bist. Wo mein Studium und meine Doktorandenzeit meine Vergangenheit widerspiegeln, bist du meine Zukunft. Ich liebe dich über alles und freue mich auf unsere gemeinsame Zeit.

Table of Contents

1	Introdu	uction	. 1
2	Metho	ds	. 6
	2.1 Direc	ct current magnetron sputtering	. 6
	2.2 Elect	tron microscopy	. 8
	2.3 Ener	gy dispersive X-ray spectroscopy	10
	2.4 X-ray	y diffraction	11
	2.5 Nano	oindentation	12
	2.6 Dens	sity functional theory	14
3	Correla	ative Experimental and Theoretical Investigation of the Angle-Resolve	ed
С	Compositio	on Evolution of Thin Films Sputtered from a Compound Mo ₂ BC Target	17
	3.1 Intro	duction	17
	3.2 Mate	erials and Methods	19
	3.2.1	Experimental details	19
	3.2.2	Simulation details	22
	3.3 Resu	ults and Discussion	26
	3.3.1	Experiment2	26
	3.3.2	Simulations	29
	3.4 Sum	mary (39

4	L	ow temperature oxidation behavior of Mo ₂ BC coatings4	٠0		
	4.1	Introduction 4	Ю		
4.2 Materials and Methods					
	4.3 Results and Discussion				
	4.4 Summary				
5	S	ynthesis and properties of orthorhombic MoAIB coatings 5	54		
	5.1 Introduction				
	5.2	Materials and Methods 5	54		
	5	.2.1 Experimental Methods 5	54		
	5	.2.2 Theoretical Methods 5	57		
	5.3 Results and Discussion 5				
	5.4	Summary 6	57		
6	С	onclusions6	8		
7	F	uture Work7	'1		
0	ח	oforonoo	7 /		

1 Introduction

To overcome the principle of trial and error in materials design, quantum mechanical calculations can be carried out to predict and explain material behavior. The research philosophy at Materials Chemistry is quantum mechanically guided materials design and vice versa, experimentally guided quantum mechanics. In this thesis, combinatorial vapor phase condensation, *ab initio* density functional theory calculations, Monte Carlo simulations and a large variety of characterization methods are utilized. Mo-B based protective coatings are investigated in this thesis, especially Mo₂BC and MoAlB, exhibit unique properties. Mo₂BC exhibits a high stiffness comparable to typical hard coatings, such as TiAlN, but in a unique combination with moderate ductility. MoAlB is reported to be the only oxidation resistant transition metal boride, forming a dense and adherent alumina scale when annealed in ambient air at 1200°C. The unit cells of orthorhombic Mo₂BC and MoAlB are shown in Figure 1.

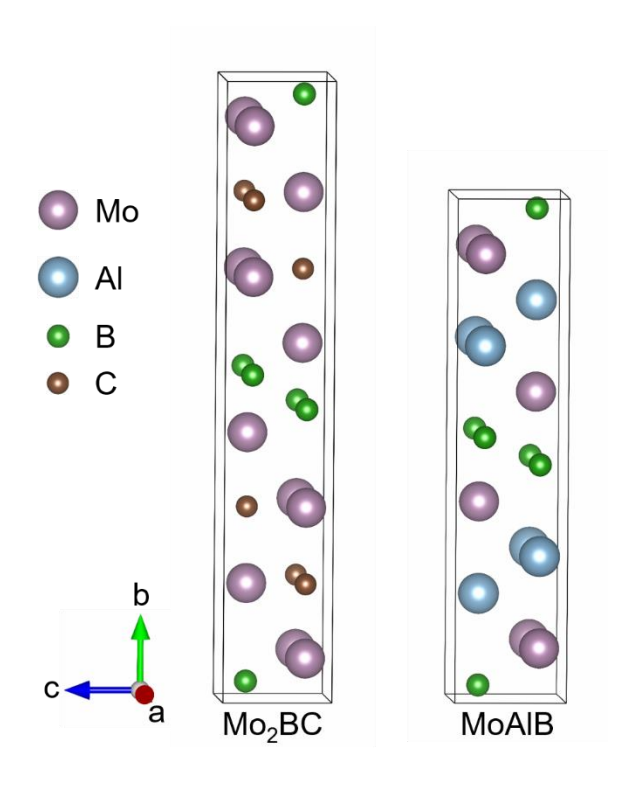


Figure 1. Unit cells of Mo2BC (left) and MoAlB (right). Cells made with VESTA [1].

In general, there are several synthesis approaches for the deposition of compound thin films. The employment of multi-elemental powder metallurgical composite targets is of great interest from an industrial application point of view due to the enhanced stability and repeatability [2]. However, it has been shown that the chemical composition of thin films deposited from multi-element targets deviate from the target composition, especially in targets with significant mass differences between their constituents, such as TiB [3, 4, 5], Cr-Al-C [6, 7], and CuZnSnSe [8]. The mass ratio of $\frac{m_{Mo}}{m_B} = 8.88$ promotes Mo₂BC to be a model system for sputter process and gas phase transport investigations, considering atomic masses of 95.96 amu and 10.81 amu for Mo and B, respectively [9]. In section 3, the angle-resolved composition evolution of Mo-B-C thin films sputtered from a Mo₂BC compound target was investigated experimentally and theoretically based on the influence of gas type on sputter process and gas phase transport.

In addition, Mo₂BC exhibits a high Young's modulus and a hardness of 460 GPa ± 21 GPa and 29 GPa ± 2GPa [10], respectively, which is comparable to hard coatings, such as TiN [11] and TiAlN [12]. The calculated bulk modulus of 324 GPa [10] is just 14% smaller than that of c-BN (376 GPa [13]) indicating a highly stiff material behavior. However, the property combination of high stiffness and hardness is often associated with brittle material behavior. Crack formation and propagation reduce coating and tool life time [14]. Materials with a property combination of high stiffness and ductility are therefore of great importance, and this is where Mo₂BC stands out, as it is additionally predicted to be moderately ductile [10].

As indicators for ductility, the ratio of bulk modulus to shear modulus (B/G) [15] and the Cauchy pressure [16] are used in literature frequently. The B/G ratio of 1.74, corresponding to the least malleable face centered cubic metal Iridium [15], is often used as critical value. B/G values larger or smaller than 1.74 are associated with ductile or brittle material behavior, respectively. The Cauchy pressure for elastic isotropic materials is defined as C₁₂-C₄₄, where C_{ij} are elastic constants [16]. For orthorhombic materials systems, exhibiting lower symmetry than cubic systems, directional Cauchy pressures can be defined as C₁₂-C₆₆, C₁₃-C₅₅, and C₂₃-C₄₄ for the (001), (010), and (100) planes, respectively. For Mo₂BC, a calculated B/G ratio of 1.73 and two positive Cauchy pressures predict moderate ductility [17]. The absence of cracks in the pile up after nanoindentation [10] as well as low crack densities in Mo₂BC coatings on Cu substrates after tensile testing [18] support these predictions.

In addition to the mechanical properties, the material performance in harsh environments, such as air at elevated temperatures during application, has to be

considered. Metallic materials forming a protective layer with a main constituent of Al₂O₃, Cr₂O₃ or SiO₂ are reported to reach acceptable lifetime in oxidizing atmosphere [19, 20, 21]. As Mo₂BC is not part of the material group forming the before mentioned protective oxide scales, oxidation is considered to be the limiting factor in application. Low tool surface temperatures of 127 and 196°C during machining of solid wood and particleboards, respectively [22], eliminate corrosion and oxidation as main wear mechanism [23]. As the tool life time of utilized cemented tungsten carbide tools is reduced by abrasion and micro-fracture during solid wood and particleboard machining [23], the utilization of Mo₂BC as a protective coating is discussed based on the low temperature oxidation behavior in section 4.

In contrast, MoAlB is reported to be the only known oxidation resistant transition metal boride, forming a dense and adherent alumina scale [24]. The first synthesis of orthorhombic bulk MoAlB was reported by Rieger *et al.* in 1965 [25]. Kota *et al.* studied the oxidation behavior of bulk MoAlB produced by hot pressing from MoB and Al powders at 1200°C for 5h [24]. While the application at high temperatures of most transition metal borides is hampered by their limited oxidation resistance above 1200°C [26, 27], MoAlB forms a protective Al₂O₃ layer [24], was reported to be capable of self-healing [28] and hence, holds great promise as high temperature material [24, 28, 29, 30]. A low mismatch in coefficient of thermal expansion (CTE) of MoAlB ($CTE_{MoAlB} = 9.5 \times 10^{-6} K^{-1}$ [24]) and α -alumina ($CTE_{alumina} = 8.5 \times 10^{-6} K^{-1}$ [31]) indicates good adhesion of the oxide scale at high temperatures as a result of low thermal stress. Recently the self-healing potential of MoAlB, the ability of "healing" by filling cracks with oxidation products, was reported and cracks in the order of 1-3 mm were healed by annealing a bulk MoAlB sample for 4 h

at 1200°C restoring the initial material strength [28]. For similar healing conditions, Ti₂AlC was reported to fill cracks already after 2 h with a mixture of TiO₂ and Al₂O₃ [32]. The unique combination of these outstanding properties suggests MoAlB in application as protective coating. In section 5 we report the synthesis of orthorhombic MoAlB coatings for the first time and compare the oxidation behavior at 1200°C to literature reports for bulk material [28, 29] and Ti₂AlC [32, 33].

2 Methods

2.1 Direct current magnetron sputtering

Direct current magnetron sputtering (DCMS) is a physical vapor deposition (PVD) technique commonly employed for thin film synthesis. A single or multiple target(s), of the material which will be vaporized, are placed inside a deposition chamber under vacuum. A negative voltage in the order of several 100 Volts is applied between target material and chamber wall or specific anodes. Typically, Ar gas, which does not react with the targets, is introduced into the chamber. Ionized Ar+ is attracted and accelerated by the negative electric field towards the target surface. Momentum transfer from Ar+ to target atoms can lead to atom and secondary electron ejection, the so-called sputter process. Permanent magnets installed below the target surface increase the effective flight distance of electrons, thereby increasing the probability to further ionize Ar within the gas phase. Hence, as compared to a glow discharge, a relatively low Ar pressure can be utilized within DCMS, resulting in a larger average sputtered particle energy arriving at the substrate surface, caused by a lower number of collisions. With a lower pressure, less gas is consumed. Therefore, systems with magnets reduce overall gas requirement. The sputter process is schematically illustrated in Figure 2.

Depending on the energy and mass of sputtered species as well as target composition (single element, composite or compound) the preferential sputter direction, also referred to as angular distribution function (ADF), can vary.

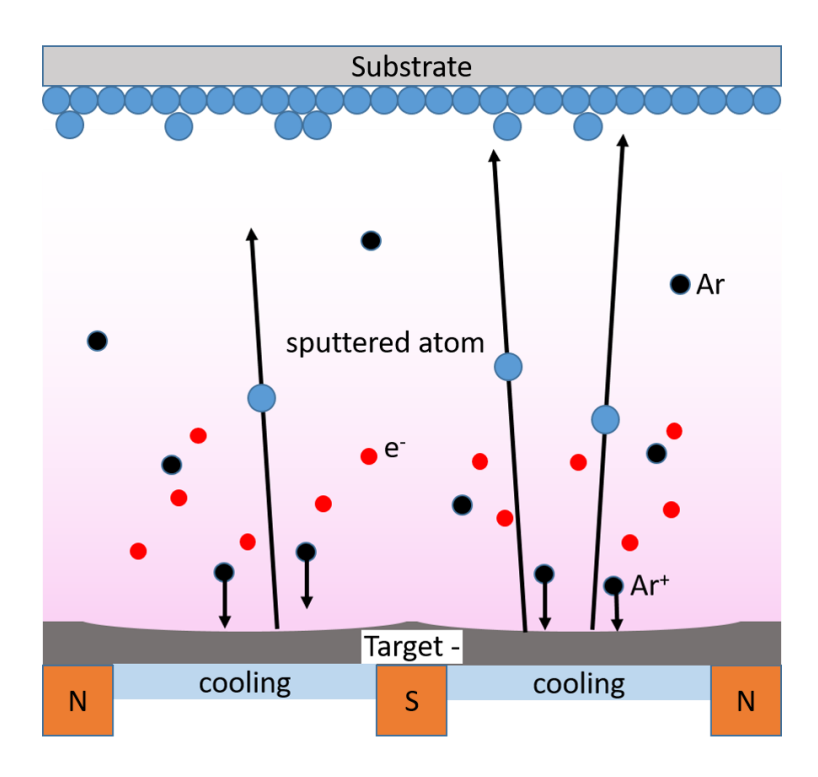


Figure 2. Schematic sputter PVD process with Ar.

For normal incident of energetic ions to the target surface, the ADF follows a cosine distribution [34]. When a multi-element compound target is sputtered, the ADF strongly dependents on the mass of the individual atoms. Light elements are preferentially sputtered to large angles with respect to the target normal as result of backscatter events on heavier atoms in the sputter cascade [35]. A detailed study on the mass dependent ADF and gas phase transport is discussed in section 3.

2.2 Electron microscopy

Scanning electron microscopy (SEM), transmission electron microscopy (TEM) and the combined scanning transmission electron microscopy (STEM) are conventional microscopy techniques used today for high resolution analysis. The maximal magnification of a standard light optical microscope is limited by the wavelength of visible light. Within an electron microscope, the wavelength of the electrons, also referred to as de Broglie wavelength, can be adjusted by applying a certain acceleration voltage, which is in the order of 2 kV to 30 kV in a conventional SEM and can be up to several hundred kV in a TEM. For this purpose, free electrons are emitted from the cathode material by either increasing the cathode's temperature and support thermally activated emission or applying an electrical field to reduce the required work-function (activation energy) and electron tunneling distance through the potential barrier. Subsequently, the emitted electrons are accelerated by an acceleration voltage, afterwards focused in a stacked system of apertures and inhomogeneous electromagnetic lenses and final directed to a defined position on a sample surface. The primary electron beam now interacts with the sample and a variety of new signals are emitted. A schematic overview of the generated signals is illustrated in Figure 3. In the conventional SEM backscattered primary electrons (BSE), newly created secondary- (SE) and auger electrons (AE) as well as photons and light can be detected and processed. The probability of the primary electron beam being backscattered increases with atomic number Z within the sample. As a result, a contrast based on atomic weight of samples constituents can be observed. Secondary electrons are ejected as result of an ionization of sample atoms. The probability of signals being detected increases with proximity of the SE generation to the sample surface as SE generated deep in the sample may be consumed by recombination. SE are mainly used for imaging as the surface topography can be displayed. AE are typically used in auger electron spectroscopy (AES) which is a method for surface chemical composition quantification [36]. The generation and detection of photons will be discussed in the subtopic energy dispersive X-ray spectroscopy (EDS).

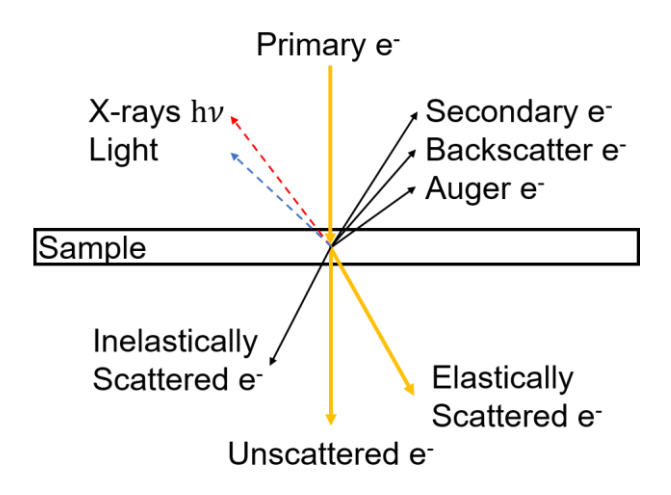


Figure 3. Schematic illustration of different signals created in electron microscopy.

In TEM and STEM the sample thickness is ideally thinner than the mean free path of the electrons enabling electron transmission. Here, unscattered electrons and elastically or inelastically scattered electrons can be detected additionally. The unscattered and elastically scattered electrons are typically used for imaging in the so call bright field (unscattered electrons) and dark field (elastic scattered electrons) mode, respectively. An additional lens in-between sample and detector in TEM allows determination of diffraction patterns which are used for structural analysis. More details on diffraction are discussed in the subtopic X-ray diffraction (XRD). Inelastically scattered electrons experience an atom specific loss in energy which can be characterized by electron energy loss spectroscopy (EELS) to determine compositional and electronic information. More information can be found in [37].

2.3 Energy dispersive X-ray spectroscopy

Energy dispersive X-ray spectroscopy is a tool for chemical quantification of a sample and typically performed in a SEM. Primary electrons transfer kinetic energy to electrons of sample atoms leading to ionization. The vacant electron site is energetically unfavored and will be occupied by an electron from a higher atomic shell. This transition, the electron jump from its higher shell to the lower shell, is associated with a release in energy which will be emitted as photon. The ratio of produced photons per ionized shell is referred to as fluorescence yield [37]. The fluorescence yield strongly depends on the atomic number and ionized shell. For C K-shell the yield is approximately 0.005 and increases to near unity for the heaviest elements [37]. In other words, 200 C K-shell ionizations result in the emittance of one photon. A further challenge in light element quantification is the photon absorption. Monte Carlo electron trajectory simulations of C K in Fe₃C with 40° take-off angle (direction of the detector) at 15 kV acceleration voltage result in 97% absorption of as-generated photons [37]. An additional obstacle for low energy photons is, if present, the window in front of the detector, protecting the detector from condensation and contamination, which can absorb photons. More detailed information can be found in [37]. To partially overcome the low accuracy of light element quantification, the EDS system can be calibrated with a sample of known composition, a so called standard. For this, the standard is quantified with other, for light elements more accurate methods such as time of flight elastic recoil detection analysis (ToF-ERDA). More detailed information can be found in [36].

2.4 X-ray diffraction

X-ray diffraction (XRD) is a common method for crystal structure analysis. The generated X-rays interact with a sample, can be diffracted and are finally detected. With the same mechanism as discussed in the method part of the energy dispersive X-ray spectroscopy in 2.3, X-rays are generated in a X-ray tube and focused by apertures on a certain position on the sample surface. Interaction of the X-rays with the sample leads to so called X-ray diffraction, which strongly depends on the atomic arrangement within the sample. If the phase shift of the diffracted X-rays is equal to n times the wavelength ($n \in \mathbb{N}$), constructive interference can be observed, leading to a strong signal in a specific angular direction which can be detected with a semiconductor detector. The specific angular direction depends on the geometry of the experimental setup and crystal structure of the sample. A correlation of crystal structure and fulfillment of constructive interference is given by Bragg's law, where $n \in \mathbb{N}$, λ is the wavelength of the X-ray, d_{hkl} is the lattice spacing of the lattice plane with the miller indices hkl and θ is the incident angle.

$$n\lambda = 2d_{hkl}\sin(\Theta) \tag{1}$$

Depending on the crystal symmetry, the experimentally determined lattice spacing d_{hkl} can be translated into lattice vectors of the crystal unit cell under consideration that the miller indices are correctly indicated. For orthorhombic materials system treated in this work, the following relationship of d_{hkl} to lattice parameters a, b, and c is valid.

$$\frac{1}{d_{hkl}^2} = \frac{h^2}{a^2} + \frac{k^2}{b^2} + \frac{l^2}{c^2} \tag{2}$$

More detailed information can be found in [38].

2.5 Nanoindentation

Materials can be tested mechanically by Nanoindentation (NI) to determine the hardness H and Young's modulus E. While a sample is indented typically with a diamond tip of predefined geometry, the load-displacement curve is determined. A schematic load-displacement curve is shown in Figure 4. While loading, the load P and displacement h increase to their maximum values, P_{max} and h_{max} , respectively. Contrary to the loading segment, where plastic and elastic deformation takes place, only elastic deformation can be reversed in the unloading segment. Hence, the reduced modulus E_{red} , which considers elastic deformation of both, indenter and sample, can be determined from the slope of the upper portion of the unloading segment [39] indicated in Figure 4 and used in Equation 3 where A_c is the projected area of the elastic contact.

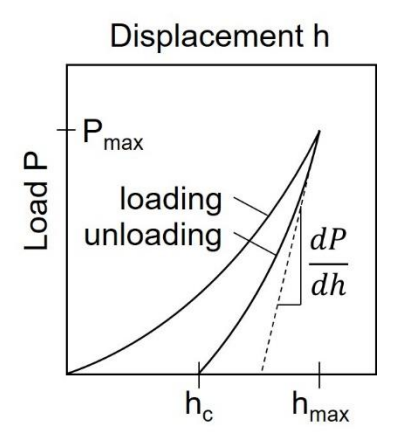


Figure 4. Schematic load-displacement curve.

$$\frac{dP}{dh} = E_{red} \frac{2\sqrt{A_c}}{\sqrt{\pi}} \tag{3}$$

For the correlation of contact area A_c and contact depth h_c the so called tip area function has to be determined. The tip area function is calibrated with a material with known Young's modulus, such as fused silica (SiO₂) with a Young's modulus of 72.5 GPa [40].

The relation of the Young's moduli of indenter and sample to the reduced modulus is given in Equation 4, where ν is the poisson's ratio and E the Young's modulus. The indices s and i represent sample and indenter, respectively.

$$\frac{1}{E_{red}} = \frac{(1 - v_s^2)}{E_s} + \frac{(1 - v_i^2)}{E_i} \tag{4}$$

Finally, the load displacement curves can be evaluated and the Young's modulus of the sample can be calculated. Additionally, the hardness H of the sample can be calculated with Equation 5.

$$H = \frac{P_{max}}{A_c} \tag{5}$$

2.6 Density functional theory

Ab initio based density functional theory (DFT) can be applied to calculate the electronic structure of a material at 0 K. Here the wording *ab initio* is the Latin term for "from the beginning" and its practical relevance in materials science is the absence of a requirement for any input parameters. The time independent Schrödinger equation (Equation 6) has to be solved where H is the Hamiltonian, Ψ the wave function and E the energy eigenvalue.

$$H\Psi = E\Psi \tag{6}$$

The electronic structure at 0 K corresponds to the ground state of the respective material. Fitting the total energy with respect to volume (by variation of lattice parameters) and applying e.g. the Birch Murnaghan equation of states (EOS) [41, 42] the ground state equilibrium lattice parameter and bulk modulus can be calculated. Additionally, elastic properties of a material can be determined by monitoring the distortion of the unit cell and the resulting changes in total energy. For orthorhombic material systems treated in this thesis, 9 independent elastic constants Cii need to be calculated, where i and j range from 1 to 6. Ravindran et al. [43] derived, based on a Taylor expansion of the internal energy of a crystal as function of strain, required distortions to calculate the elastic constants. Subsequently, the elastic constants can be used to calculate polycrystalline bulk modulus (B), shear modulus (G), Young's modulus (E) and Poisson's ratio (ν). As a polycrystal is an assemble of randomly oriented monocrystals, the description of the stress and strain distribution when applying an external load might be challenging. In 1929 and 1952 solutions for this problem were published by establishing extreme cases: considering a uniform strain (Voigt approximation) [44] or a uniform stress (Reuss approximation) [45] in the polycrystal.

Voigt and Reuss bulk moduli (B_V and B_R) and shear moduli (G_V and G_R) can be calculated by Equation 7 to 10, where C_{ij} are the elastic constants and S_{ij} are the elastic compliance constants. It is important to note that the matrix product of the elastic constant matrix C and the compliance matrix S result in the identity matrix I.

$$B_V = \frac{1}{9}(C_{11} + C_{22} + C_{33}) + \frac{2}{9}(C_{12} + C_{13} + C_{23})$$
 (7)

$$B_R = \frac{1}{(S_{11} + S_{22} + S_{33}) + 2(S_{12} + S_{13} + S_{23})}$$
(8)

$$G_V = \frac{1}{15}(C_{11} + C_{22} + C_{33} - C_{12} - C_{13} - C_{23}) + \frac{1}{5}(C_{44} + C_{55} + C_{66})$$
(9)

$$G_R = \frac{15}{4(S_{11} + S_{22} + S_{33} - S_{12} - S_{13} - S_{23}) + 3(S_{44} + S_{55} + S_{66})}$$
(10)

Hill et al. [46] proved with energetic considerations that the before discussed extreme cases are the upper and lower limit of the real polycrystalline elastic moduli and proposed to describe a real polycrystal by the arithmetic average of the extremes (Equations 11 and 12).

$$B = \frac{1}{2}(B_V + B_R) \tag{11}$$

$$G = \frac{1}{2}(G_V + G_R) \tag{12}$$

Considering the correlation of elastic properties in an isotropic material, which is valid for a random polycrystal, the Young's modulus and Poisson's ratio can be calculated with the following equations:

$$E = \frac{9BG}{3B+G} \tag{13}$$

$$\nu = \frac{3B - 2G}{2(3B + G)} \tag{14}$$

All calculation parameters are presented in the method parts of the respective sections.

3 Correlative Experimental and Theoretical Investigation of the Angle-Resolved Composition Evolution of Thin Films Sputtered from a Compound Mo₂BC Target

3.1 Introduction

Mo₂BC is classified as a nanolaminated material with orthorhombic structure [10, 47, 48]. It shows a unique combination of mechanical properties, such as an elastic modulus of 470 GPa, a ratio of bulk and shear moduli of 1.73, and a positive Cauchy pressure, which are required for hard and wear-resistant coatings with moderate ductility [10, 17]. Bolvardi *et al.* [49] successfully synthesized crystalline Mo₂BC at 380 °C by high power pulse magnetron sputtering (HPPMS) [50] as compared to a required temperature of 580 °C during direct current magnetron sputtering (DCMS) [51]. The lower deposition temperature for synthesis of a crystalline thin film by HPPMS was attributed to a larger adatom mobility induced by ion bombardment during HPPMS.

There are several synthesis approaches for the deposition of compound thin films, such as the utilization of reactive gases [51], co-sputtering from several targets [52, 53], or targets with plugs [54]. Likewise, the employment of multi-elemental powder metallurgical composite targets is of great interest from an industrial application point of view due to the enhanced stability and repeatability [2] of non-reactive sputtering compared to reactive sputtering processes. However, it has been shown that the chemical composition of thin films deposited from multi-element targets deviate from the target composition, especially in targets with significant mass differences between their constituents, such as TiB [3, 4, 5], TiW [55, 56, 57, 58, 59, 60, 61, 62], WB [63], SiC [64], MoSi [65, 66], VC [67], NbC [68], Cr-Al-C [6], Ti₂AlC [69], and Ti₃SiC₂ [70, 71]. The

difference in the chemical film composition was attributed to several mechanisms: (i) the mass and size differences of the target constituents and the respectively associated different angular and energy distribution functions (EDF) of the sputtered species [3, 6, 35, 65, 66], (ii) their mean free paths as well as the energy transfer in collisions with the sputtering gas during transport [3, 4, 6, 35, 55, 61], and (iii) different sticking coefficients and re-sputtering of the film constituents by backscattered Ar [55, 56, 57, 58, 59, 60].

The compositional evolution of binary Ti-B thin films was investigated experimentally and with a Monte Carlo model based on TRIDYN (dynamic transport of ions in matter) and TRIM (transport of ions in matter) codes [3]. It was shown that the Ti/B ratio strongly depends on the gas pressure and target-substrate distance, which in product is proportional to the number of collisions sputtered species experience within the gas phase. The model was extended to Cr-Al-C thin films – a ternary system [6].

Van Aeken *et al.* [72] developed a Monte Carlo code SIMTRA for the simulation of sputtered particle trajectories in a gas-phase within a definable 3D setup. Collision modelling by interatomic potentials and thermal motion of background atoms are included within the code.

From the above, it can be learned that the deviation of the chemical composition of thin film and multi-element target can be controlled by the sputtering pressure and gas type.

Within this work, experimental data were compared to a model based on TRIDYN and SIMTRA utilized for Mo-B-C thin films to understand how the gas phase transport affects the thin film chemical composition in a system with large mass differences of the multi-element target constituents.

3.2 Materials and Methods

3.2.1 Experimental details

Mo-B-C thin films were deposited in a high vacuum chamber assembled from a DN160 six-way cross. A base pressure of $< 1.1 \, x \, 10^{-4} Pa$ was achieved before all depositions with a combination of a rotary-vane (Edwards E2M28) and a turbomolecular pump (Pfeiffer Vacuum TPU 240). A self-built magnetron with Ø 90 mm was placed in the center of the chamber. A 6 mm thick Mo₂BC compound target (Plansee Composite Materials GmbH) with the composition of 54.3, 24.2, and 21.5 at. % of Mo, B, and C, respectively, bonded on a Cu backing-plate was utilized for the investigations. The target contains a major Mo₂BC phase with minor Mo₂C and MoC phases (Figure 5) as measured by a Bruker D8 Discovery general area detector diffraction system (GADDS) with Cu(K α) radiation at 40 kV and 40 mA with a constant incident angle of ω =15°.

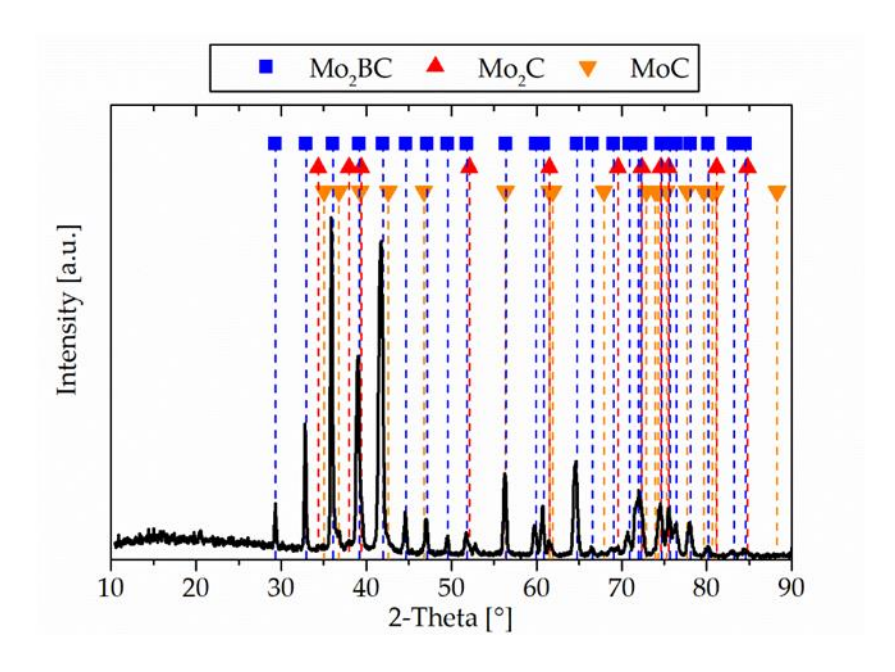


Figure 5. XRD pattern of the powder-metallurgically manufactured Mo2BC compound target. Small phase fractions of Mo₂C and MoC were detected.

Figure 1. XRD pattern of the powder-metallurgically manufactured Mo₂BC compound target. Small phase fractions of Mo₂C and MoC were detected.

The thin films were deposited for 1 hour onto grounded not intentionally heated Si (100) substrates with a size of approximately 15 x 15 mm² arranged at different angular positions with respect to the target normal of $\alpha \in \{0^{\circ}, \pm 22.5^{\circ}, \pm 45^{\circ}, \pm 67,5^{\circ}\}$ (Figure 6). The target-substrate distance was kept constant at 70 mm with respect to the target center point. The DC power of 100 W was applied by an ADL 1.5kW DC power supply. The Ar and Kr pressures utilized in the depositions are summarized in Table 1.

Table 1. Ar and Kr gas pressures and measured target voltages which correspond to impinging ion energies for Ar⁺ and Kr⁺ ions

Argon		Krypton	
Pressure (Pa)	Voltage (V)	Pressure (Pa)	Voltage (V)
0.09	401	0.09	441
0.27	344	0.26	423
0.46	328	0.45	421
0.66	324	0.64	418
0.98	314	0.96	403

The chemical composition of the deposited films was measured by energy dispersive X-ray spectroscopy (EDX) attached to a JEOL JSM-6480 scanning electron microscope (SEM). The electron gun of the SEM was operated at an acceleration voltage of 5 kV.

Each sample was measured 10 times. The statistical uncertainty associated with this EDX quantification of Mo, B, and C was less or equal 5% relative deviation. To overcome the unknown systematic uncertainty for light elements in EDX, the samples deposited at 0.66 Pa Ar with $\alpha = 0^{\circ}$, -22.5°, -45°, and -67.5° were quantified by time-of-flight elastic recoil detection analysis (ToF-ERDA) and used as a standard for the respective positions. The statistical uncertainty for all ToF-ERDA was < 0.4% absolute. In ToF-ERDA, the relative systematic uncertainties in the specific energy loss of the constituents and primary ions of the target are assumed to range from 5 to 10%. Hence, the lower bound of the total measurement uncertainty for the EDX analysis with ToF-ERDA quantified standards ranges from 7 to 11%.

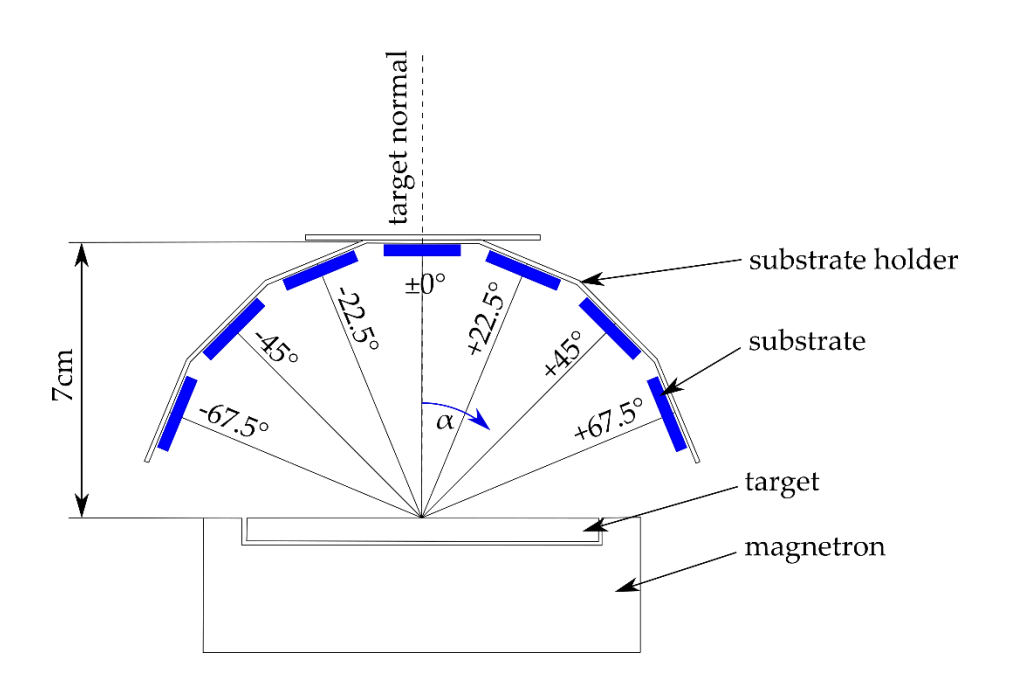


Figure 6. Experimental setup with seven substrates positioned at $\alpha \in \{0^{\circ}, \pm 22.5^{\circ}, \pm 45^{\circ}, \pm 67,5^{\circ}\}$ angle arrangement with respect to the target normal and a target-substrate distance of approximately 70 mm.

3.2.2 Simulation details

The angular-resolved chemical composition of the thin films was simulated with a Monte Carlo model based on TRIDYN [73, 74] and SIMTRA [72] for the sputtering process and the gas phase transport, respectively.

3.2.2.1 TRIDYN

The impinging ion energies of Ar⁺ and Kr⁺ ions in the TRIDYN simulation were set according the experimentally measured target voltages (Table 1). To address the dependence of the surface binding energy from the surface chemistry, a matrix model was introduced [74] and modified [6] for a system containing three elements as presented in Equation 15, where SBE_i is the surface binding energy of the i-th target element at a given target concentration c, c_i is the concentration of the i-th target element, and SBV_{i-j} is the surface binding potential of the i-th and the j-th elements. SBV_{i-j} are assumed to be constant. Calculated angular distribution functions (ADF) and energy distribution functions (EDF) of the sputtered species are utilized in SIMTRA.

$$\begin{pmatrix}
SBE_{Mo} \\
SBE_{B} \\
SBE_{C}
\end{pmatrix} = \begin{pmatrix}
SBV_{Mo-Mo} & SBV_{Mo-B} & SBV_{Mo-C} \\
SBV_{B-Mo} & SBV_{B-B} & SBV_{B-C} \\
SBV_{C-Mo} & SBV_{C-B} & SBV_{C-C}
\end{pmatrix} \begin{pmatrix}
c_{Mo} \\
c_{B} \\
c_{C}
\end{pmatrix}.$$
(15)

For the determination of the surface binding potentials, an approach based on the energy conservation law [6, 74] was used and will in the following be called energy conservation law approach. In addition, a DFT *ab initio* based approach has been employed.

3.2.2.2 Energy conservation law approach

The surface binding potential of pure elements SBV_{i-i} is assumed to be equal to the enthalpy of sublimation $\Delta_{sub}H_i$. The surface binding potential of the atom pairs SBV_{i-j} is calculated using Equation 16, where $\Delta_f H_{Mo_nB_mC_o}$ is the enthalpy of formation of the ternary compound and a and b are the stoichiometric factors of the elements "i" and "j" .

$$SBV_{i-j} = \frac{1}{2} \left(\Delta_{sub} H_i + \Delta_{sub} H_j \right) - \frac{1}{3} \frac{n + m + o}{2ab} \Delta_f H_{Mo_n B_m C_o}$$
 (16)

The energy of formation per formula unit (f.u.) of $\Delta_f H_{Mo_2BC}$ =-1.132 $\frac{eV}{f.u.}$ used in the simulations was calculated by Bolvardi *et al.* [17]. The enthalpies of sublimation of 6.83 eV, 5.73 eV, and 7.51 eV for Mo, B, and C are given in the elements.dat file of TRIDYN, respectively. In addition, enthalpies of sublimation of 6.81 eV, 5.75 eV, and 7.37 eV for Mo, B, and C respectively can be found in [75].

3.2.2.3 *Ab initio* approach

In addition to the TRIDYN approach, an *ab initio* approach based on DFT was used for the determination of the respective surface binding potentials. DFT calculations were implemented within the Vienna *ab initio* simulation package (VASP) [76, 77]. Perdew-Burke-Ernzerhof (PBE) adjusted generalized gradient approximation (GGA) [78] was used for all calculations with projector augmented wave potential [79]. In addition, the

tetrahedron method for total energy using Blöchl-corrections [80] and the reciprocal space integration using Monkhorst-Pack scheme [81] were applied. The utilized *k*-point grid was 4x4x4 for the (100) and (001) surfaces and 6x2x6 for the (010) surface. The cut-off energy was set to 500 eV with an electronic relaxation convergence of 0.01 meV.

Considering the matrix model presented in Equation 15, the energy required to remove atoms of specific surfaces with different chemical compositions needs to be calculated. (100) and (001) surfaces as well as different surface terminations of the (010) surface are considered in the calculation are illustrated in Figure 7. Subsequently, atoms are removed from the surface creating a vacancy. The change in energy is considered to be the surface binding potential of the atom within the respective surface as shown in Equation 17. E_i is the energy of the atom i after being removed from the surface, E^{surface,j} is the energy of surface j with vacancy of atom i and E^{surface j} is the energy of the surface j without defect. Within DFT, the surfaces were simulated by a vacuum layer on top of the unit cell with the height of approximately 10Å for (100) and (001) and 17Å for (010) surfaces. Calculated SBV for both approaches are presented in Equations 18 and 19.

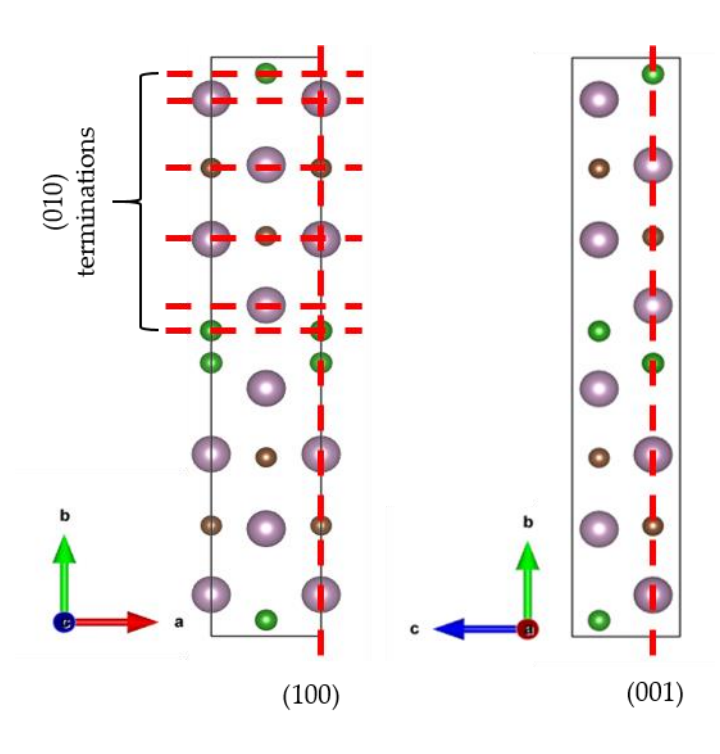


Figure 7. Considered (100), (001) surfaces and (010) surface terminations for the determination of the surface binding potentials in the ab initio approach, figure made with VESTA [1]

$$SBV_{i-j} = E_i + E_{vac,i}^{surface,j} - E^{surface,j}$$
(17)

$$SBV_{energy\ conservation\ law} = \begin{pmatrix} 6.83 & 6.66 & 7.50 \\ 6.66 & 5.73 & 7.32 \\ 7.50 & 7.32 & 7.41 \end{pmatrix} eV$$
 (18)

$$SBV_{ab initio} = \begin{pmatrix} 7.25 & 7.33 & 9.46 \\ 7.19 & 6.98 & 9.71 \\ 7.36 & 7.26 & 9.46 \end{pmatrix} eV$$
 (19)

3.2.2.4 SIMTRA

Within SIMTRA simulations, 1×10^7 particles for Mo and 5×10^6 particles for B and C corresponding to a 2:1:1 target composition were transported. For the simulation setup, a

cylinder with a diameter of 0.16 m and a length of 0.334 m was used. The target was positioned in the center of the simulation chamber. Seven circular substrates with a radius of 5 mm were arranged in the chamber corresponding to the actual experimental setup. The gas temperature was set to 300 K. The atomic interaction was described with the Lenz-Jensen screening function implemented in SIMTRA. Gas motion and diffusion is considered within the gas transport. The racetrack profile of the target used for the experimental work was measured by a profilometer and taken into account for the simulations. The simulations were carried out in vacuum ($p_{Ar} = 1 \times 10^{-9} \text{ Pa}$) and in Ar and Kr gaseous atmosphere at pressures utilized in the experiments (Table 1). Atoms redeposited on the target during deposition are not sputtered again within the simulation. To overcome this virtual loss of particles, atoms redeposited on the target are distributed on all surfaces within the utilized simulation chamber with respect to the initial particle distribution, including the influence of the angular distribution function. For this, the ratio of deposited atoms on a substrate divided by the total number of sputtered atoms was multiplied with the number of deposited atoms on the target surface and added to the specific substrate.

3.3 Results and Discussion

3.3.1 Experiment

The angle- and pressure-dependent film compositions for both sputtering gases, Ar and Kr, are presented in Figure 8. The target composition is indicated by black solid lines. For both sputter gases, the angle-dependence of Mo is convex, while the lighter elements B and C show a concave angle-dependence. At $\alpha \le 22.5^{\circ}$ (Figure 6), a deficiency of the

heavy element (Mo) and a surplus of light elements (B and C) is measured. The opposite trend is observed for $\alpha \ge 45^\circ$. Hence, the film composition while sputtering from a Mo₂BC target is angle-dependent, which was previously observed by Olsen *et al.* [35] for sputtering (metallic) alloy targets. They explained mass-dependent angular distribution functions by backscattering of light elements on the heavier elements within the collision cascade in the target [35] resulting in an enrichment of lighter elements in directions normal to the target surface. Obviously, Mo cannot be backscattered due to reflective collisions with lighter elements, such as B and C.

Comparing the Mo content of Ar and Kr depositions, a clear pressure-dependence can be seen for Kr, while no significant composition changes were obtained for Ar. For Kr sputtering at $\alpha=0^{\circ}$, the Mo content changes from 36 at. % at 0.09 Pa to 43 at. % at 0.96 Pa. The chemical variation at $\alpha=\pm45^{\circ}$ is less distinct, while at $\alpha=\pm67.5^{\circ}$, the Mo content variations are within the measurement error. For gas phase scattering of B and C in Kr, the opposite trend is observed regarding the angle-dependent composition variation. However, the chemical variations due to pressure changes are within the measurement error. It is evident that an increase in pressure leads to a chemical composition closer to the nominal target composition and hence, stoichiometry. In an effort to determine the cause for the here observed sputtering gas induced composition deviations, simulations were carried out, which allow for an independent analysis of composition deviations caused by sputtering of the target and scattering during the gas phase transport.

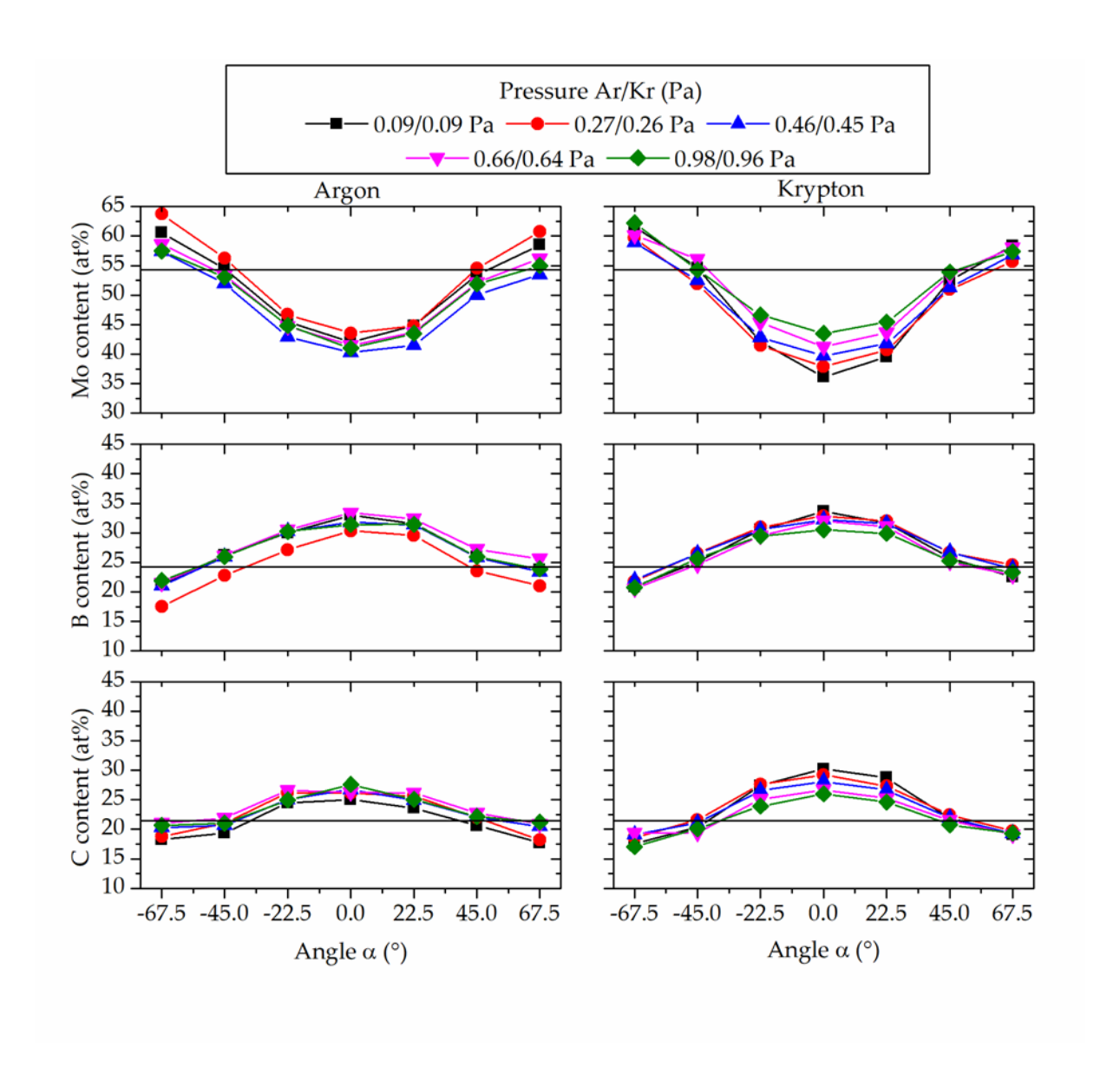


Figure 8. Angle-resolved composition evolution of the deposited thin films within the pressure range from 0.1 to 1.0 Pa. The first pressure value pertains to the Ar depositions, the second value to the Kr depositions. The average oxygen content was less than 1.5 at. % for all depositions and not considered further. The target composition is marked by the black horizontal lines.

3.3.2 Simulations

The angle- and pressure-dependent film compositions with surface binding potentials (SBV's) determined by the energy conservation law and *ab initio* approaches, as discussed above, are presented in Figure 9 for depositions in Ar.

The trend of the experimentally determined angle- and pressure-dependent film composition depicted in Figure 4 is reproduced. The angle-dependence of Mo is convex, while B and C show a concave angle-dependence. Films at $\alpha \leq 22.5^{\circ}$ exhibit a deficiency of the heavy Mo and an enrichment of light B and C. As in the experimental data for $\alpha > 45^{\circ}$, an opposite trend is observed. The maximum difference in SBV's determined by the energy conservation law and *ab initio* approaches is 32%. This SBV difference leads to composition differences of less or equal to 0.9 at. % and 1.1 at. % for Mo sputtered in Ar (Figure 9) and Kr (not shown), respectively. The magnitude of these composition differences cannot be resolved by EDX as the expected experimental errors are larger than the composition differences. For all simulations discussed below SBV's determined by the *ab initio* approach were employed.

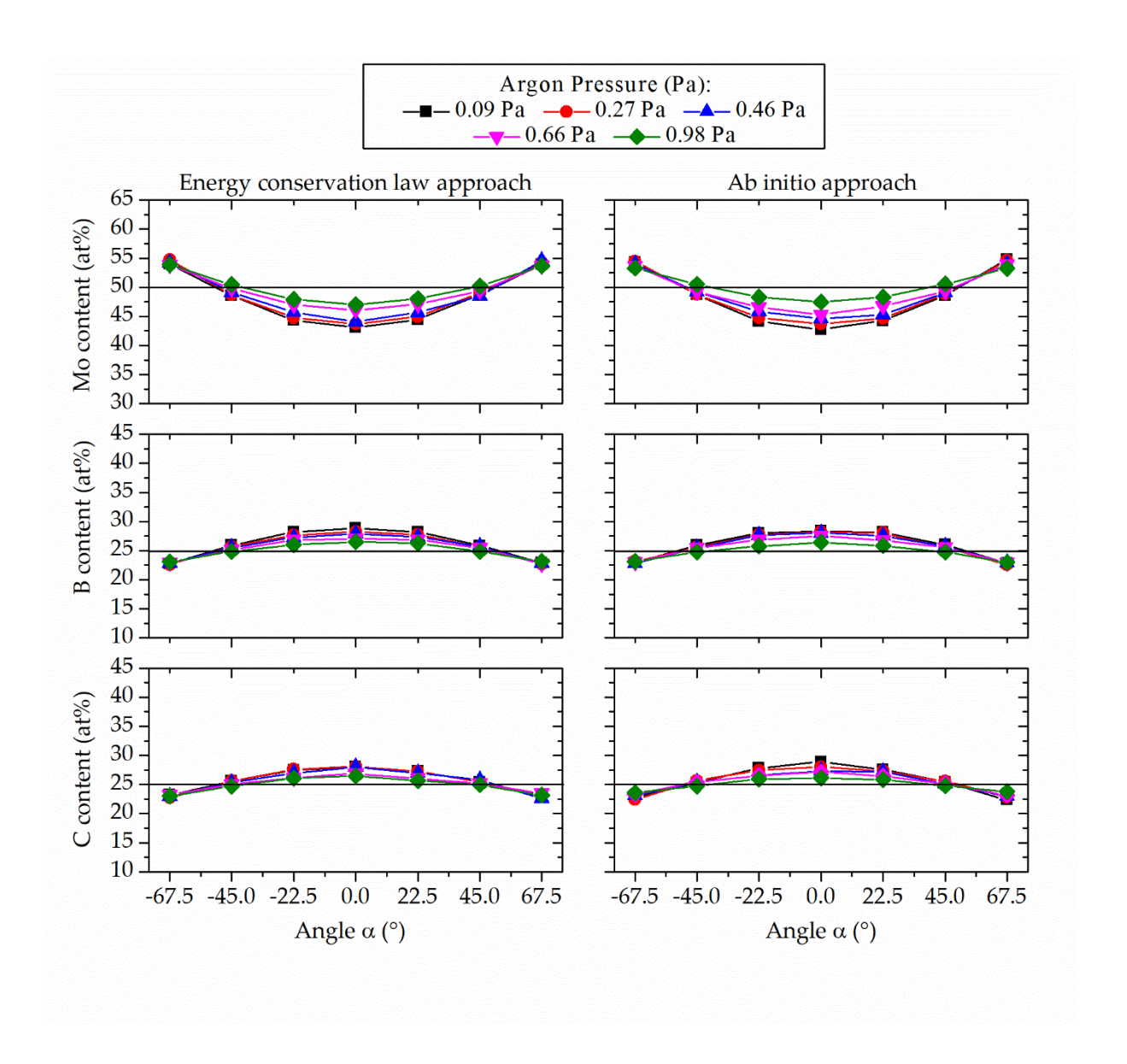


Figure 9. The simulated angle-resolved composition of thin films with the Ar pressure range from 0.09 to 0.98 Pa. Considered surface binding energies of the two approaches (left) energy conservation law and (right) ab initio. The ideal stoichiometric target composition is marked by the black horizontal lines.

Pressure changes affect the target voltage and hence the ion energies impinging on the target, see Table 1. The influence of the ion energy on the ADF is illustrated in Figure 10. Within these simulations scattering events during gas phase transport are deliberately not considered by utilizing an Ar pressure of 10⁻⁹ Pa. Hence, these simulations only

describe sputtering, specifically the effect of the kinetic energy of Ar+ and Kr+ on the angle-dependent composition of the sputtered flux. These simulations will therefore be referred to as *initial* ADF's. Increasing the kinetic energy of Ar+ from 314 eV to 401 eV (by 27%) results in absolute mean composition differences of less or equal 0.4 at. % for all simulations. Hence, the absolute, ion energy induced composition changes in the sputtered flux are on average one order of magnitude smaller than the expected measurement error and hence could not be resolved by EDX measurements.

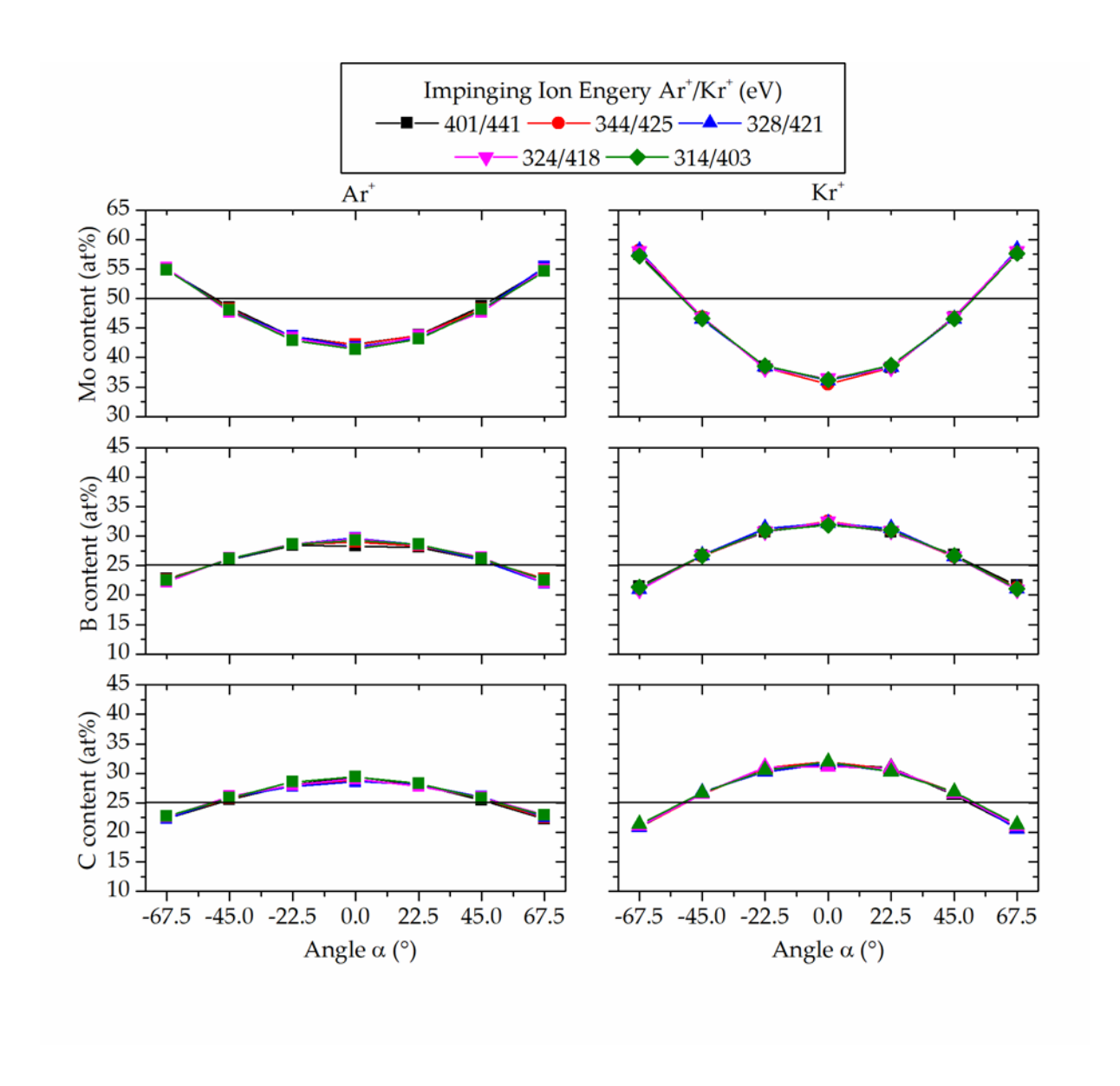


Figure 10. Angle-resolved composition evolution of the sputtered flux for different impinging ion energies of Ar+ (left) and Kr+ (right) ions. The first energy value pertains Ar+ sputtering, the second value to Kr+ sputtering. The ideal stoichiometric target composition is marked by the black horizontal lines.

The *initial* ADF of Mo sputtered by Ar⁺ (see Figure 10) exhibits a convex distribution resulting in a Mo deficiency of 8 at. % at $\alpha = 0^{\circ}$ with respect to a nominal Mo content of 50 at. %. At $\alpha = \pm 67.5^{\circ}$, a surplus of 5 at. % Mo is obtained. Both light elements exhibit a concave distribution resulting in a surplus of 4 at. % at $\alpha = 0^{\circ}$ and a deficiency of 3 at. %

at α = ±67.5° with respect to a nominal light element content of 25 at. % each. Sputtering by Kr⁺ (Figure 10) leads to more pronounced convex and concave distributions for heavy and light elements, respectively. The Mo deficiency and surplus are increased to 14 at. % and 8 at. %. For both light elements, a surplus of 7 at. % and a deficiency of 4 at. % can be found at α = 0° and ±67.5°, respectively. Compared to Ar, the sputtering induced differences of ADF in Kr result in larger deviations between the composition of the target and the angle dependent sputtered flux. These results can be rationalized based on the above discussed mass dependent reflective collisions within the target surface. In the collision cascade only B and C can be backscattered by Mo leading to a preferential ejection of B and C close to the target normal. Whereas Mo cannot be backscattered due to a reflective collision with lighter B or C.

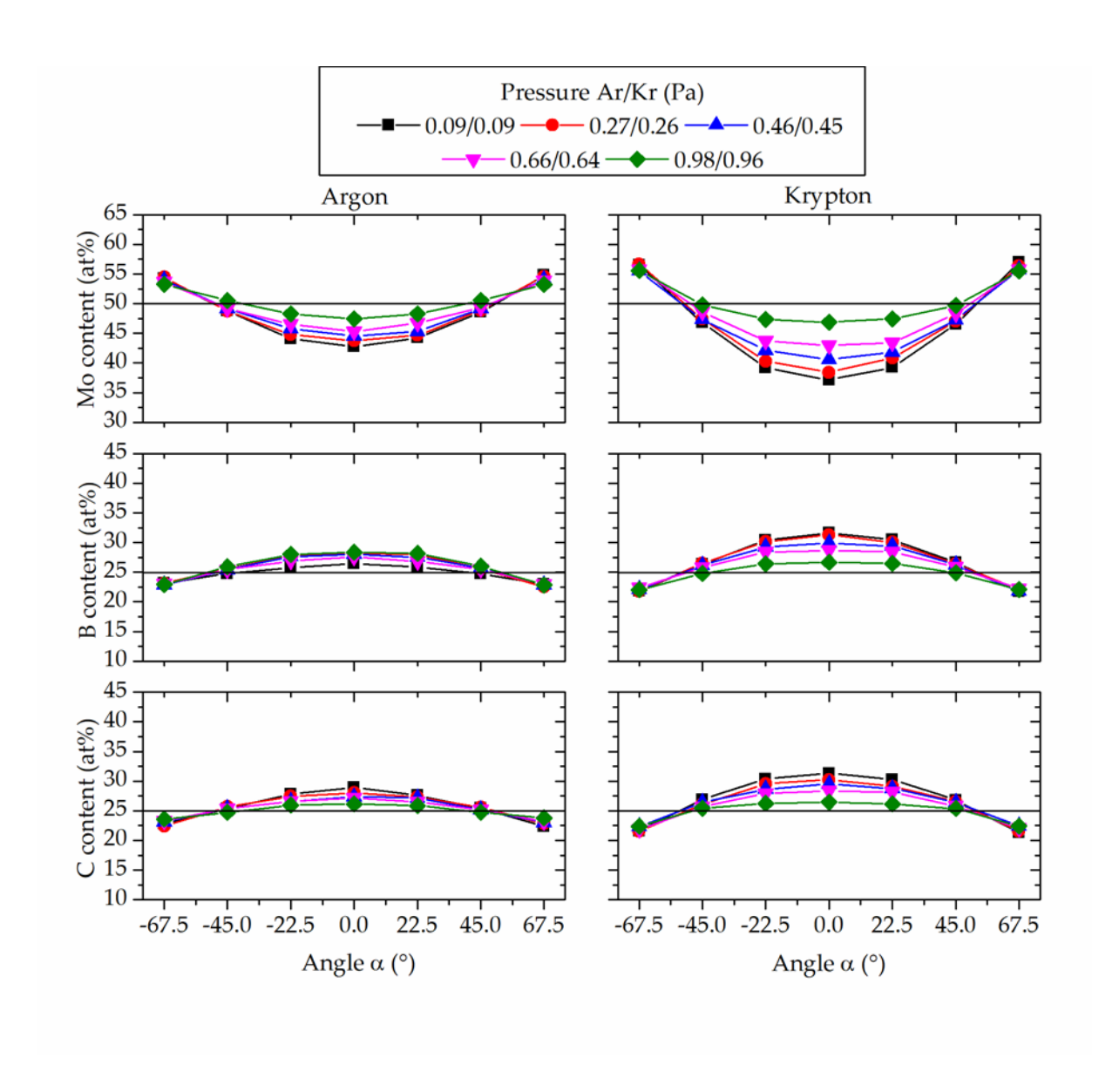


Figure 11. Angle-resolved evolution of simulated film compositions considering sputtering at the target as well as scattering during gas phase transport. The first pressure value pertains to the Ar depositions, the second value to the Kr depositions. The ideal stoichiometric target composition is marked by the black horizontal lines.

Simulations of the film composition that take in addition to sputtering at the target also the scattering events within gas phase transport into account are shown in Figure 11. The Ar or Kr pressures are identical to the experimental pressures depicted in Table 1.

Generally, the experimentally determined angle-dependent film composition data are consistent with the simulation results.

Significant differences between the initial ADF and the ADF obtained after scattering during transport in the gas phase are obtained for Kr and Ar as the pressure is increased by one order of magnitude. An increase in Mo content at $\alpha = 0^{\circ}$ of 4.7 at. % and 9.7 at. % and for both light elements a decrease of 3 at. % and 5 at. % can be obtained in Ar and Kr, respectively. At $\alpha = \pm 67.5^{\circ}$ no significant pressure induced impact on the chemical composition can be observed. Generally, the pressure induced variations in chemical composition are more pronounced in Kr and are in good agreement with the experimentally determined data. Comparison to the EDX composition measurement error indicates that the pressure-dependent composition variations simulated in Ar cannot be resolved experimentally.

To identify the cause of the here discussed angle- and pressure dependent film composition variations, the angle-resolved average trajectory lengths of the sputtered species are calculated. The average trajectory length, d, is the mean distance a particle travels from sputtering at the target to deposition at the substrate surface and is maximized for scattering events at large scattering angles and short mean free path. The pressure-dependence of d is shown in Figure 12 for Ar and Kr.

Increasing the Ar pressure by one order of magnitude results in a relative increase of d at $\alpha = 0^{\circ}$ of 59%, 31% and 42% for Mo, B and C, respectively. The same change in Kr pressure results in a relative increase of d at $\alpha = 0^{\circ}$ of 111%, 25% and 29% for Mo, B and C, respectively. Hence, the average Mo trajectory length is up to 85 % larger in Kr than in Ar.

The average number of Mo collisions at the maximum Ar and Kr pressures at $\alpha=0^\circ$ is 19.4 and 22.9 at, respectively, exhibiting a relative difference of 18.2%. As the pressure induced increase in average trajectory length d is caused by the number of collisions as well as the average scattering angle, simulations were conducted where the number of collisions was kept constant to unravel contribution of the average scattering angle. For each element one additional simulation was conducted at a specific Kr pressure (0.89 Pa for Mo and 1.10 Pa for B and C) to match the number of collisions computed for scattering in 0.98 Pa of Ar which are 19.4, 10.7 and 12.4, for Mo, B, and C, respectively.

At a constant average number of Mo collisions of 19.4 the pressure induced increase in d of Mo is 23% larger in Kr as in Ar. At an average number of collisions of 10.7 and 12.4 for B and C, respectively, a pressure induced increase in d of 1.3% and 0.7% was obtained for B and C, respectively. Hence, it is deduced that the average scattering angle of Mo is significantly larger in Kr than in Ar and that the evolution of the angle- and pressure-dependent film composition is determined by the average scattering angle of Mo. Assuming energy- and momentum conservation, a mass-dependent expression for the maximum scattering angle of a particle with a mass larger than the gas species as given by Eq. 20 [34, 82], where ϑ_{max} is the maximum scattering angle and m_{Mo} and m_i are the masses of Mo and the gas atom, respectively. Consequently, maximum scattering angles for Mo of 24.6° and 60.4° in Ar and Kr, respectively, were obtained for the masses of 95.96 amu, 39.95 amu, and 83.80 amu for Mo, Ar and Kr, respectively [9].Hence, the above deduced larger average scattering angles for Mo in Kr as compared to Ar are caused by the mass ratio between the sputtering gas and Mo.

$$\vartheta_{\text{max}} = \arcsin\left(\frac{m_{\text{gas}}}{m_{\text{Mo}}}\right)$$
 (20)

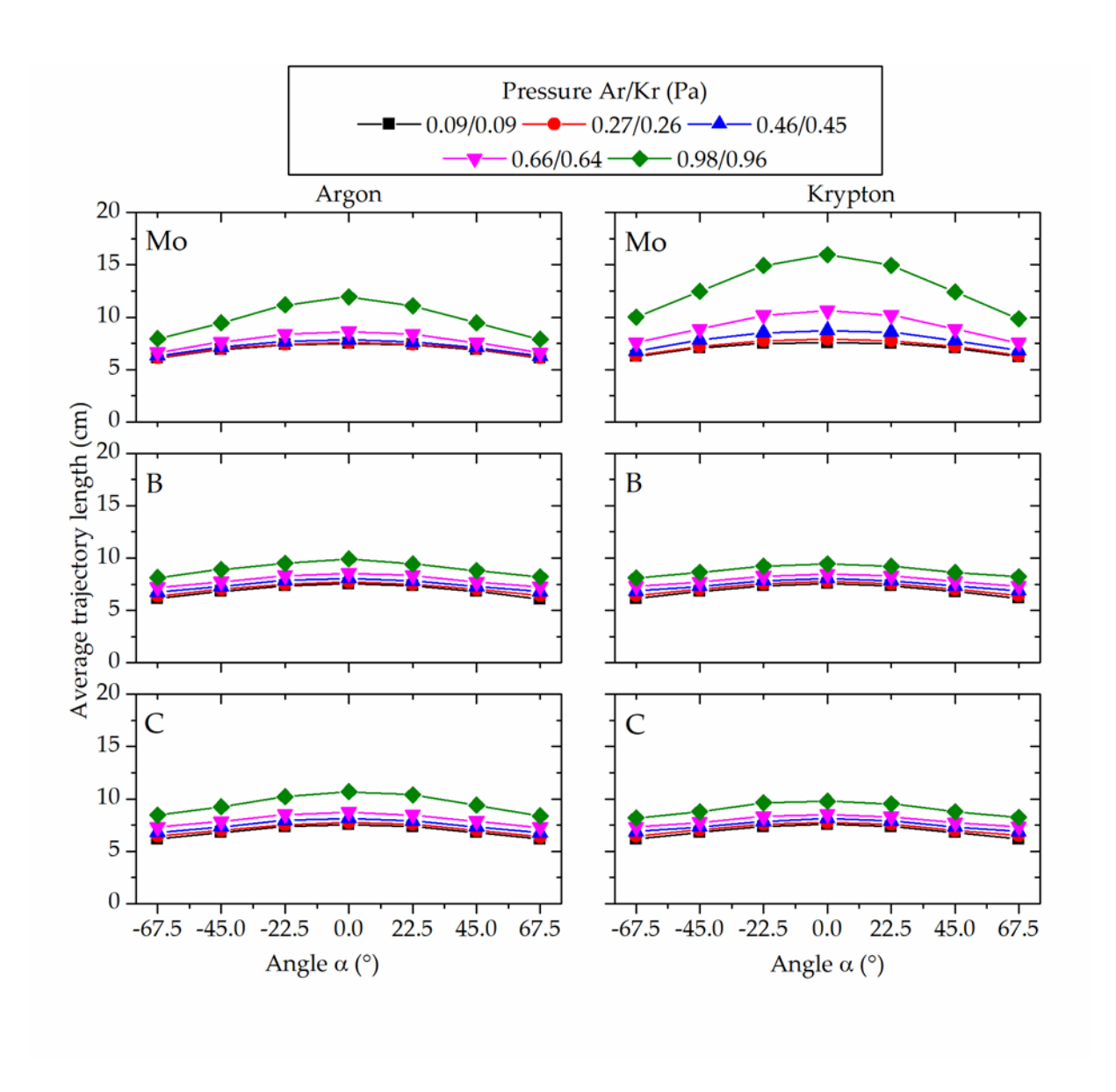


Figure 12. Simulated average trajectory length of the sputtered atoms transported through the gas phase at given Ar (left) and Krypton (right) pressures. The first pressure value pertains to the Ar depositions, the second value to the Kr depositions.

The simulations carried out within this work allowed independent consideration of the sputtering process at the target surface as well as the scattering events within the gas

phase transport. Pressure variations over one order of magnitude insignificantly influence the sputtering process, whereas the mass of the impinging ion exhibits a strong impact on the initial ADF. Sputtering induced differences between the target and thin film composition caused by Kr⁺ are larger compared to sputtering with Ar⁺, which is in agreement with the sputtering experiments at low pressures.

Gas phase scattering events induced variations in film chemical composition depend on both, the gas pressure and mass of the gas atom. The average trajectory length was shown to be a good indicator for the impact of scattering. To unravel the relative contribution of numbers of collision and average scatter angle simulation with identical number of collisions in Ar and Kr of 19.4, 10.7 and 12.4, for Mo, B, and C, respectively were conducted. In Kr compared to Ar a dominant pressure induced increase in *d* of 69% for Mo, compared to 1.3% and 0.7% for B, and C, respectively, was obtained. Hence, the significantly larger average trajectory length of Mo in Kr as compared to Ar at the same number of collisions can be rationalized by the larger average scattering angle of Mo which in turn controls the evolution of the angle- and pressure-dependent film composition.

3.4 Summary

The angle-resolved composition evolution of Mo-B-C thin films deposited from a Mo₂BC compound target was investigated. While the Ar and Kr pressure was varied, the samples were positioned in a specific angular arrangement with respect to the target normal with a target substrate distance of 7 cm. Since B and C, as light elements, can only be backscattered on the heavy Mo, a concave angular distribution was obtained as consequence of reflective collisions. Contrary, a concave angular distribution for Mo was observed. Sputtering with Kr⁺ leads to significant deviations between target and thin film composition. An increase in Ar pressure by one order of magnitude does not affect the angle-resolved composition. As the Kr pressure is increased, significantly more effective scattering in Kr leads to a thin film composition which is closer to the target composition. The average trajectory length, which is influenced by the effective number of collisions and the scatter angle in each collision, is used as a parameter to characterizes the effectiveness of scattering in Ar and Kr. A significantly larger average trajectory length of Mo in Kr compared to Ar was obtained. The mass ratio between sputtering gas and sputtered species is shown to define the scattering angle within the collision cascade in the target and in the gas phase transport, which ultimately defines the angle- and pressure-dependent film composition.

4 Low temperature oxidation behavior of Mo₂BC coatings

4.1 Introduction

Solid wood and particleboards are typically machined with cemented tungsten carbide tools [22, 83, 84]. Especially Oil Palm Empty-Fruit Bunch (OPEFB) particleboards are reported to be one of the most abrasive materials for cutting tools due to its high silica content [23]. Steady-state cutting tool surface temperatures in the range of 127 to 196°C, for solid wood and OPEFB particleboards, respectively, are reported [22]. Mechanical abrasion and micro-fracture were identified as main wear mechanism for cemented tungsten carbide tools [23]. Additionally, temperature induced softening of the cobalt matrix, already appearing at 127°C and subsequent eventual removal of hard carbide particles is reported as wear mechanism reducing the life time of the unprotected cemented tungsten carbide tools [22].

The utilization of protective coatings with comparable high stiffness and hardness is a path to increase tool lifetime. However, the property combination of high stiffness and high hardness is often associated with brittle material behavior. Crack formation and propagation reduce coating and tool lifetime [14]. Recent literature promotes Mo₂BC based on its predicted unique property combination of high stiffness and moderate ductility as protective coating [10, 85, 86]. The calculated bulk modulus of 324 GPa [10] is just 14% smaller than that of c-BN (376 GPa [13]) indicating highly stiff material behavior. Additionally, Mo₂BC is predicted to be moderately ductile based on a calculated B/G ratio of 1.73 and two positive Cauchy pressures [17]. The absence of cracks in the pile up after

nanoindentation [10] as well as low crack densities in Mo₂BC coatings on Cu substrates after tensile testing [18] support these predictions.

The thermal stability of Mo₂BC coatings was recently investigated and the formation of a secondary Mo₂C phase was found between 900 and 1000°C [87, 88]. Differences in the Mo₂C phase formation temperature are speculated to be the result of slight off-stoichiometry in the as-deposited films [87]. Nonetheless, an increase in stiffness and hardness associated with crystallization and grain growth of Mo₂BC films annealed in vacuum up to 1000°C were reported [87, 88].

Bolvardi *et al.* [89] theoretically investigated the interaction of Al with an O-exposed Mo₂BC (040) surface and theoretically described the onset of Al adhesion. No further oxidation studies of Mo₂BC, neither bulk nor coatings, are reported. The oxidation behavior of Mo rods was investigated by Gulbransen *et al.* [90] and the formation of a MoO₃ volatizing partially at 600°C at 76 Torr (0.1 Bar) was found. Kota *et al.* [29] investigated the oxidation of bulk MoAlB and no evidence for the formation of crystalline B₂O₃ at 1200°C was observed as an amorphous oxide layer may have been formed or the formed B₂O₃ layer may have evaporated during the annealing experiment as B₂O₃ is volatile above 1100°C [91]. During oxidation of Ti₂AlC, a release of CO₂ from 200°C onwards and additionally CO at temperatures higher 800°C was reported by Zhang *et al.* [92]. The oxidation behavior in ambient air at elevated temperatures may limit the application of Mo₂BC as protective coating and hence, needs to be investigated.

4.2 Materials and Methods

Mo₂BC coatings were deposited by combinatorial direct current magnetron sputtering in a high vacuum lab scale deposition system as presented in [10]. Mo, B₄C and C targets with 50 mm in diameter were operated with power densities of 2, 2.8 and 6.1 W/cm², respectively. As substrate material, Al₂O₃ (0001) wafers pre-coated with an approximately 550 nm thin TiN adhesion layer were utilized. The TiN adhesion layer was synthesized by cathodic arc deposition using three Ti targets. The substrates were heated to 450 °C and the nitrogen pressure was kept constant at 3.0 Pa during deposition onto the floating substrates. The TiN coated Al₂O₃ substrate were heated to approximately 900°C with a heating rate of 20 K/min and held at this temperature for 30 min to homogenize the temperature distribution prior to Mo₂BC deposition. The deposition was carried out in Ar with a pressure of 0.27 Pa. The target-to-substrate distance was 10 cm and the deposition time was 240 min resulting in a film thickness of ~1.5 μm. A floating potential of approximately -10 V was measured during deposition and the substrates were rotated at a speed of 15 rpm. Substrate cooling rate was 10 K/min after deposition.

Oxidation experiments were performed in a GERO (F 40-200/13) tube furnace in ambient air. The samples and a thermocouple were placed in an Al₂O₃ crucible and put into the furnace. Isochronal oxidations were conducted for 15 min in a temperature range from 100 to 500°C. In addition, samples were annealed up to 28 days and 14 days at 100 and at 200°C, respectively, corresponding to steady-state cutting tool surface temperatures for machining of solid wood and particleboards [22].

The thin film cross-sectional microstructure was characterized using scanning transmission electron microscopy (STEM) in a FEI HELIOS Nanolab 660 dual-beam

focused ion beam (FIB) microscope (Hillsboro, OR, USA) operating with a STEM III detector at acceleration voltage and current of 30 kV and 50 pA, respectively. In order to obtain thin lamellae for the characterization, a 1 µm thick Pt protection layer was deposited with 80 pA current on the region of interest followed by trench milling using Ga⁺ ions accelerated with a voltage of 30 kV. The lamellae were consequently extracted by using a manipulation needle and attached to a Cu Omniprobe. Subsequent thinning was performed utilizing currents of 0.79, 0.43 ,0.23 nA and 80 pA to acquire final lamellae thicknesses below 100 nm.

Energy dispersive X-ray spectroscopy (EDX) line-scan analyses on thin lamellae were performed using an EDAX TEAM™ system equipped with an Octane Elect EDX detector for chemical analysis with an acceleration voltage of 5 kV, current of 0.8 nA, and a step size of 5 nm.

Chemical composition depth profiles were obtained by Time-of-Flight elastic recoil detection analysis (ToF-ERDA) at the tandem accelerator laboratory of Uppsala University. Recoils were generated by using 36 MeV ¹²⁷l⁸⁺ projectiles and measured with a solid-state detector. A detailed description of the detection systems can be found in[93]. Systematic uncertainties may result in up to 10% relative deviation of absolute concentration values with the origin in the electronic stopping of projectile and recoiling species and detection efficiencies < 1 for light elements [94, 95]. However, systematic uncertainties are expected to be identical for all investigated thin films as they were analyzed in one measurement batch. Hence, the systematic uncertainties do not affect the relative comparison of depth profiles.

Finally, the as-deposited (a.d.) and oxidized coating structures were investigated with a Bruker D8 Discovery general area detector diffraction system (GADDS) with a grazing incidence angle of 10°using Cu (Kα) radiation and the voltage and current were 40 kV and 40 mA, respectively.

4.3 Results and Discussion

BF-STEM cross-sections of FIB lamellae and qualitative EDX line scans of the a.d. state and samples isochronally oxidized for 15 min in a temperature range from 250°C to 500°C are shown in Figure 13. BF-STEM and EDX line scans were performed on these samples to determine the oxide scale thickness, morphological changes and qualitative compositional distribution along the film thickness. While sample holder exchange from FIB to STEM the lamellae were exposed to atmosphere and hence, it is reasonable to assume that the measured oxygen content of the lamellae is larger than in the as deposited coating.

The samples oxidized for 15 min at 250 and 300°C exhibit no detectable oxide scale. Oxidation for 15 min at 350°C results in the formation of an oxide scale with a thickness of 42 ± 3 nm as shown in Figure 13 (d). The samples oxidized at 400 and 500°C exhibit oxide scale thicknesses of 75 ± 8 nm and 278 ± 29 nm, respectively. Furthermore, no oxidation induced changes in Mo₂BC morphology are observed but first crystalline features in the oxide scale of the sample oxidized at 500°C can be seen. For all samples, the variation of Mo and B along the film thickness is within the measurement precision. The slight decrease in C content along the film thickness for the samples oxidized at temperatures ≥250°C may be attributed to CO₂ release during the oxidation process which was previously reported for Ti₂AlC starting at 200°C [92].

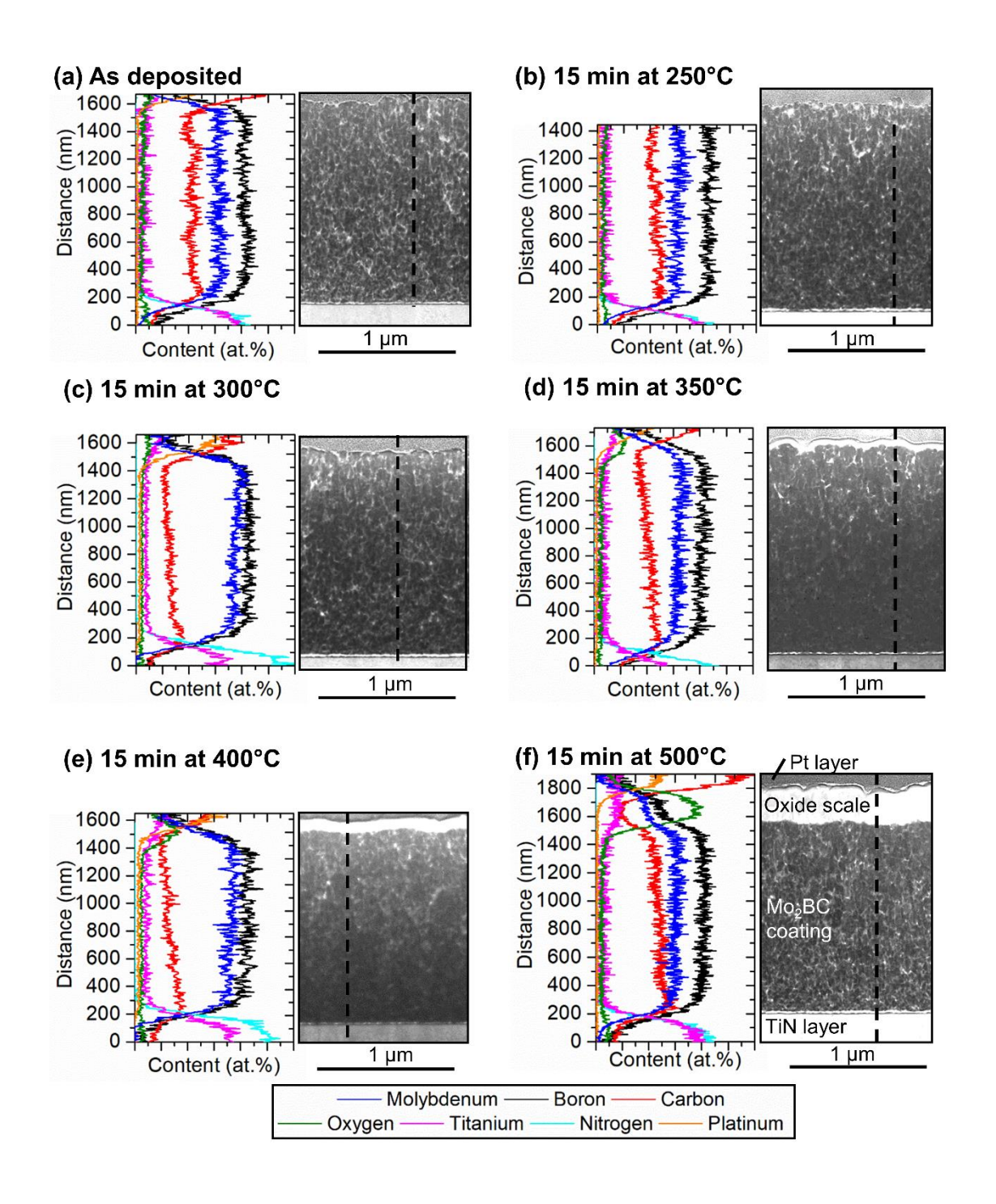


Figure 13. BF-STEM cross-section and qualitative EDX line scan of as deposited sample (a), samples isochronally oxidized for 15 min at 250°C (b), 300°C (c), 350°C (d), 400°C (e) and 500 °C (f). The dashed black line indicates the position of the line scan. After STEM on (b) the protective Pt layer was lost, hence the line scan was stopped before reaching the edge of the sample.

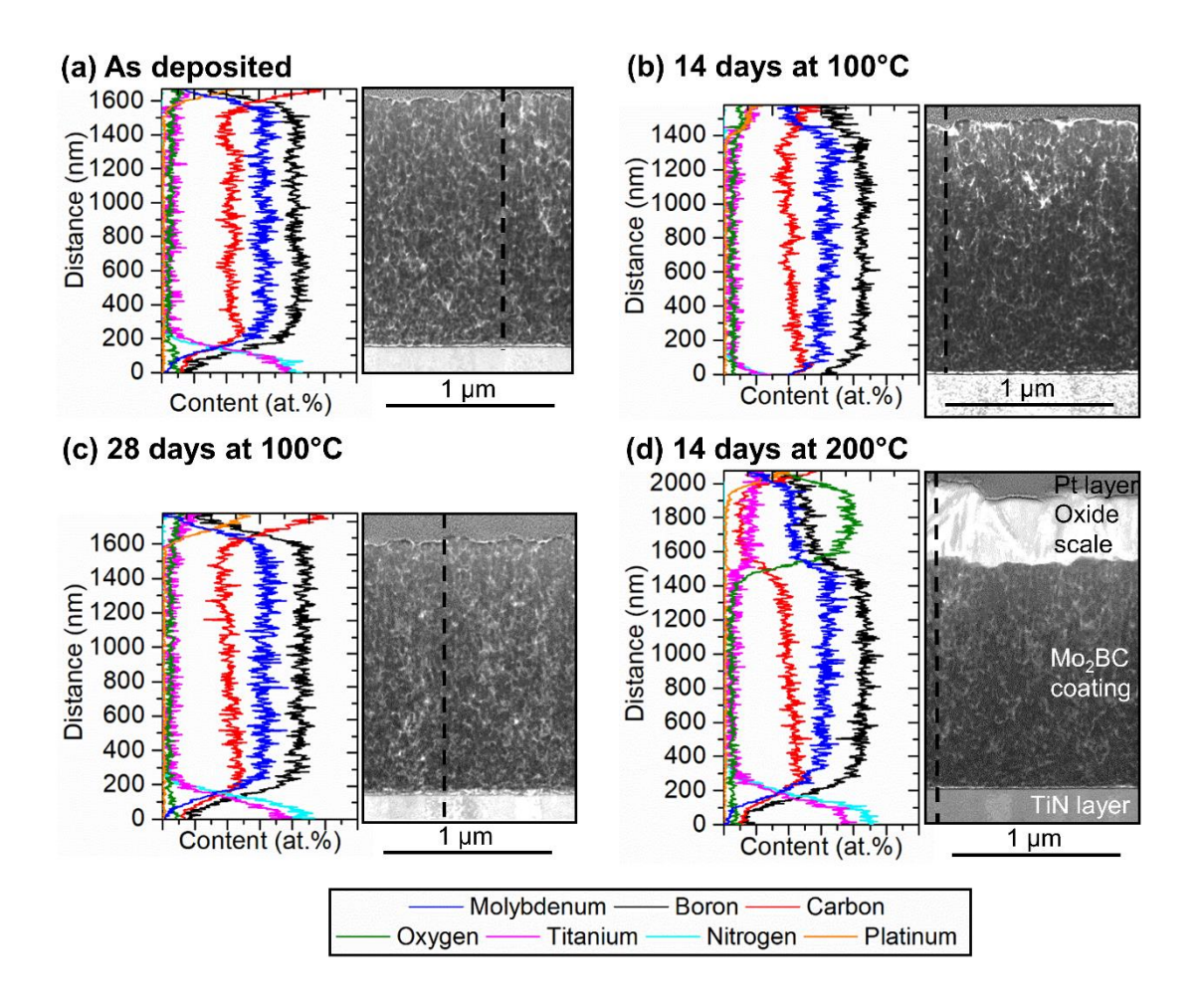


Figure 14. BF-STEM cross-section and qualitative EDX line scan of as deposited sample (a), samples isothermally oxidized for 14 days (b) and 28 days (c) at 100°C and for 14 days at 200°C (d). The dashed black line indicates the position of the line scan.

BF-STEM cross-sections of FIB lamellae and qualitative EDX line scans of the as deposited state and samples isothermally oxidized for 14 and 28 days at 100°C and 14 days at 200°C are shown in Figure 14. The sample oxidized for 14 days at 100°C exhibits a scale thickness of 22 nm ± 10 nm which corresponds to only 5% of the oxide scale thickness of 401 ± 33 nm formed after 14 days at 200°C. After 28 days at 100°C an oxide scale thickness of 13 nm ± 3 nm was measured. Consistently with the isochronally oxidized samples no morphological changes in Mo₂BC are observed. Similarly to the

isochronal oxidation experiments the distribution of Mo and B concentrations along the coating thickness is within the expected measurement error. The slight decrease in C content for the isothermally oxidized samples may, as in the isochronal experiments, be due to CO₂ release during the oxidation process which was previously reported for Ti₂AlC starting at 200°C [92]. As the sample oxidized for 15 min at 500°C features in the oxide scale indicating crystallinity are observed for the sample oxidized for 14 days at 200°C. All samples in Figure 13 and Figure 14 exhibit a comparable oxygen profile in the Mo₂BC matrix to the as deposited state. Hence, oxygen is insignificantly diffusing in the sample while oxidation for 15 min up 500°C and while 28 days and 14 days oxidation at 100°C and 200°C, respectively.

For the as-deposited state a composition of 44 at.% \pm 4.4 at.% Mo, 23 at.% \pm 2.3 at.% B and 33 at% \pm 3.3 at.% C corresponding to a nominal stoichiometry of Mo₂B_{1.05}C_{1.5} was determined by ToF-ERDA. The oxygen areal density determined by ToF-ERDA of the as deposited sample and samples oxidized in ambient air isochronally for 15 min in a temperature range from 100 to 500°C and samples isothermally annealed for 1 to 14 days at 200°C are shown in Figure 15. For isochronally oxidized samples, the onset of oxidation was identified after 15 min at 300°C as the surface oxygen content exhibits a significant increase from 3 at.% in the as deposited state to 14 at.% by a factor of 4.6 as shown in Figure 15 (a). Further increase to oxidation temperatures of up to 400°C is associated with a gradual increase in oxide thickness. At 500°C the oxide scale persists of 73 at.% O and 24 at.% Mo (not shown) which fits to stoichiometric MoO₃. Slight deviations from the ideal stoichiometry are attributed to impurities and residual B and C. For all isothermally oxidized samples a gradual decrease in oxygen content along the depth profile is

observed. After oxidation for 10 and 14 days a composition of approximately 70 at.% O and 24 at.% Mo (not shown), fitting to stoichiometric MoO₃, was observed.

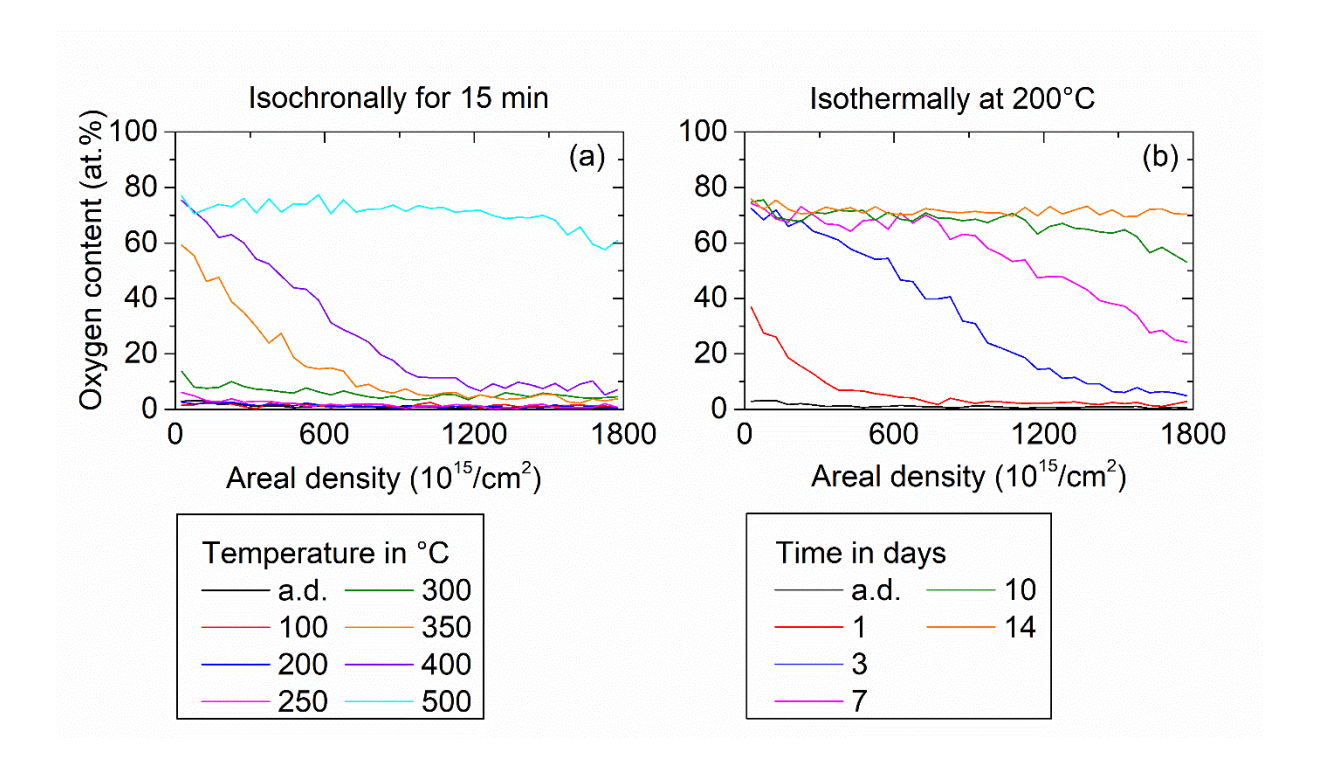


Figure 15. Oxygen areal density of as deposited sample, samples oxidized in ambient air isochronally for 15 min in a temperature range from 100 to 500°C in (a) and samples isothermally annealed for 1 to 14 days at 200°C in (b).

X-ray diffraction data of the as deposited sample and samples isochronally oxidized for 15 min in a temperature range from 250 to 500°C are plotted in Figure 16. The coating structure was studies by comparing lattice plane peaks with the International Center of Diffraction Data database using powder diffraction files (PDF). All diffraction data of samples isochronally oxidized for 15 min up to 400°C can be attributed to orthorhombic Mo₂BC (00-029-0913). After 15 min oxidation at 500°C additional peaks, attributed to orthorhombic MoO₃ (00-035-0609) were observed and are in excellent agreement with

the MoO₃ stoichiometry determined by ToF-ERDA and morphological features identified in STEM indicating crystallinity in the oxide scale.

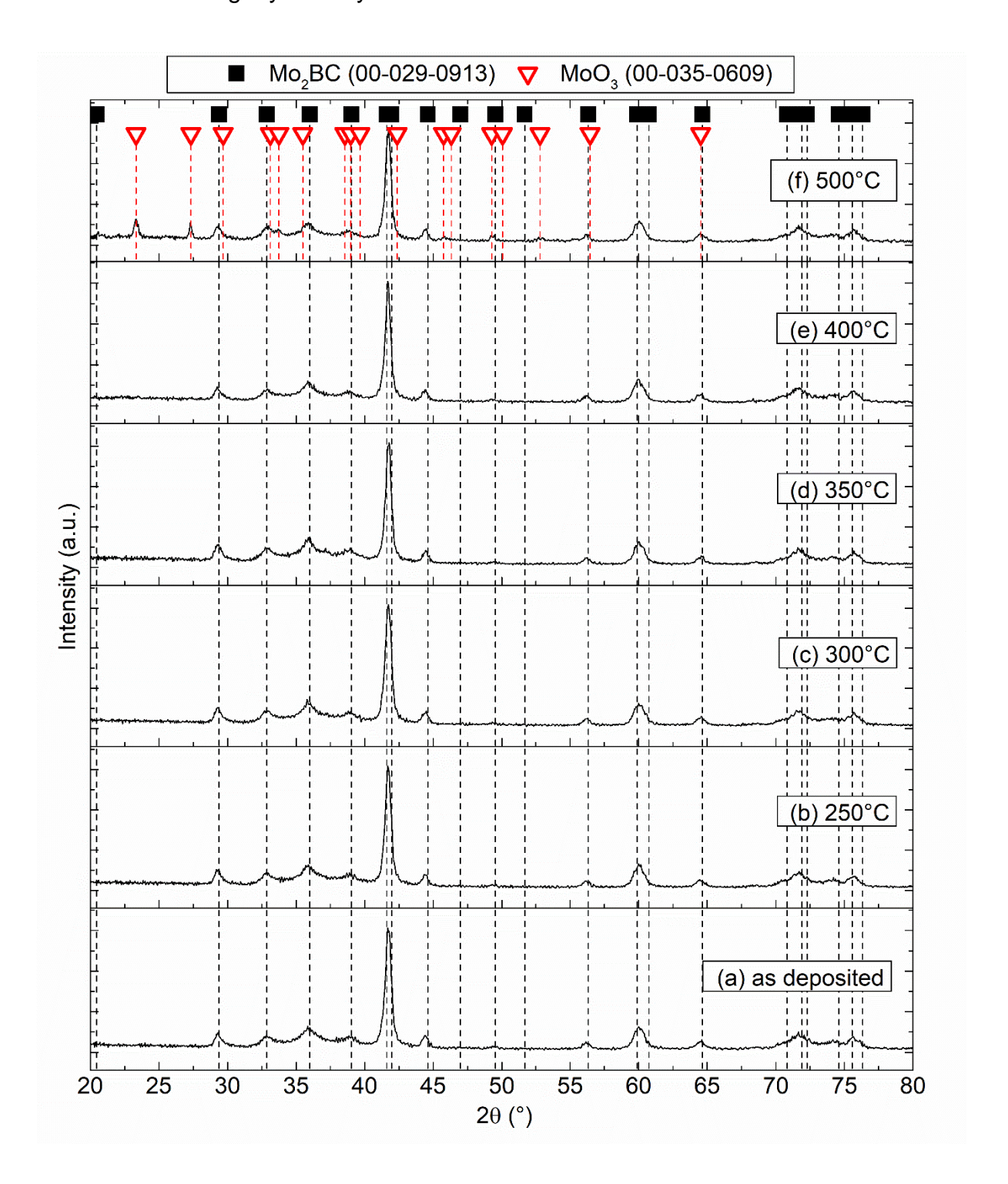


Figure 16. Diffraction data of as deposited sample (a), samples isochronally oxidized for 15 min at 250°C (b), 300°C (c), 350°C (d), 400°C (e) and 500 °C (f).

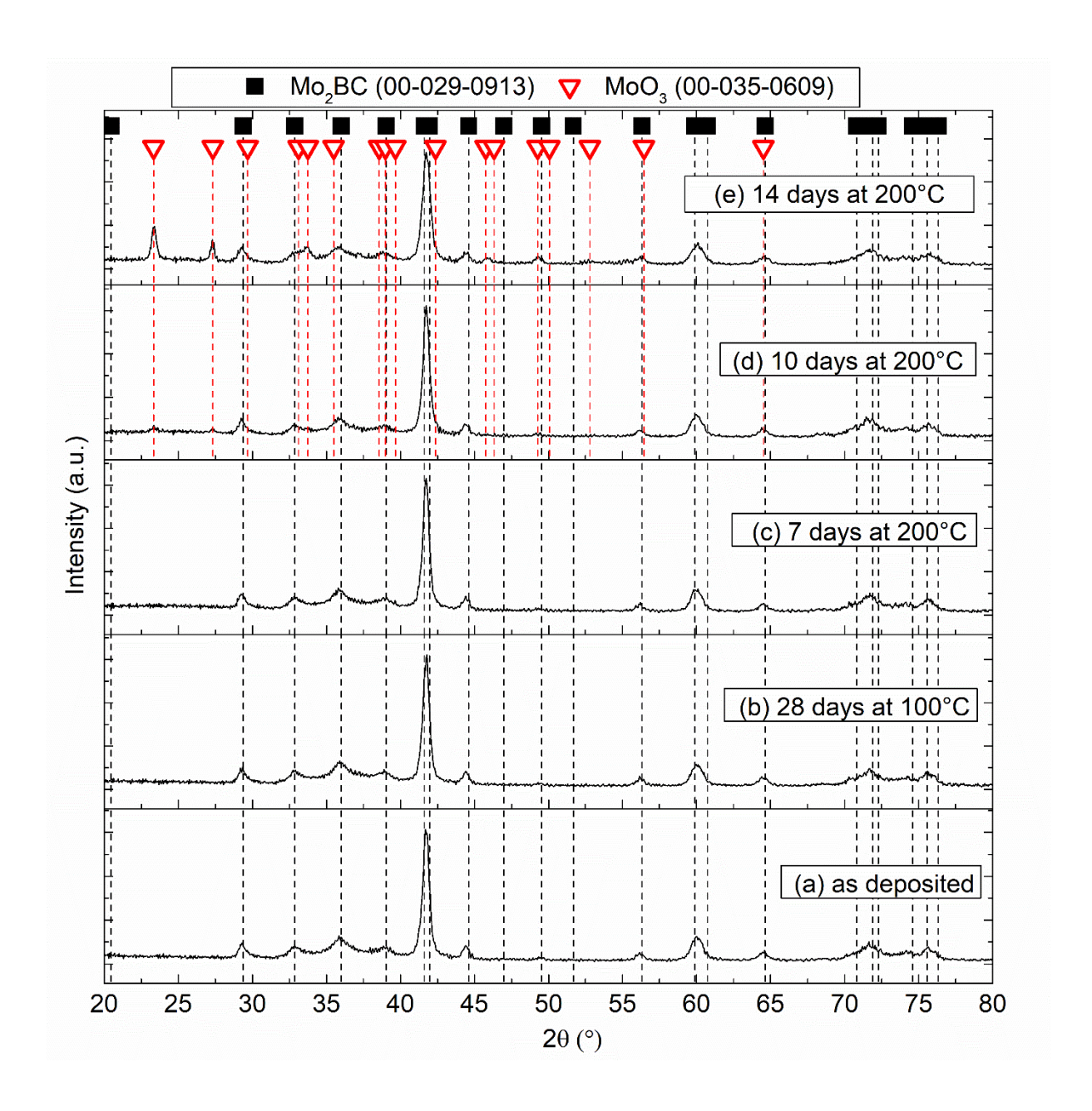


Figure 17. Diffraction data of as deposited sample (a), samples isothermally oxidized for 28 days at 100°C (b) and for 7 days (c), 10 days (d) and 14 days (e) at 200°C, respectively.

X-ray diffraction data of the as deposited sample and samples isothermally oxidized for 28 days at 100°C and 7 to 14 days at 200°C are plotted in Figure 17. The diffraction patterns of the samples oxidized for 28 days at 100°C and for 7 days at 200°C are comparable to the as deposited state. After oxidation for 10 days and 14 days at 200°C

additional peaks, attributed to the formation of orthorhombic MoO₃ (00-035-0609) were observed. Additionally, the identified MoO₃ is in excellent agreement with the composition data determined by ToF-ERDA and morphological features identified by STEM indicating crystallinity in the oxide scale comparable to the sample oxidized for 15 min at 500°C.

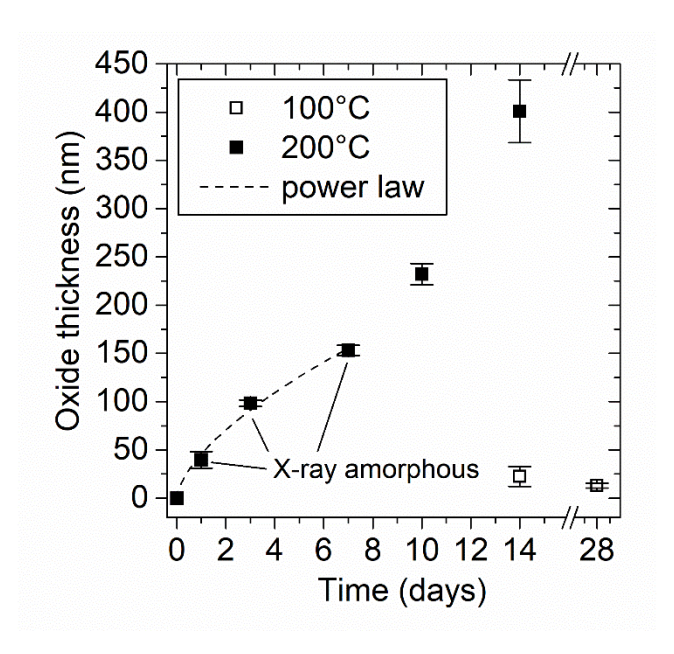


Figure 18. Oxide scale thickness formed on Mo₂BC coatings oxidized at 100°C and 200°C. White symbols belong to 100°C while black symbols belong to 200°C. The dashed black line was calculated based on X-ray amorphous oxide scale appearing at 200°C for oxidation times up to 7 days.

The oxide scale thickness formed on Mo_2BC coatings during oxidation at $100^{\circ}C$ and $200^{\circ}C$ as a function of the oxidation time is shown in Figure 18. For $200^{\circ}C$ isothermal oxidation a power factor of n = 0.63 was calculated based on the oxidation behavior of the X-ray amorphous samples with a correlation coefficient of 0.985. Crystallinity in the oxide scales, observed for the coatings oxidized for 10 and 14 days, exhibit significant thicker scales as the extrapolated power law. Hence, the increase in scale thickness and the

associated kinetics at 200°C after 8 days appears to be associated with the crystallization of the initially X-ray amorphous oxide scale as shown by X-ray diffraction (Figure 17).

For the here investigated oxidation scenarios MoO₃ was the only crystalline low temperature oxidation product observed after oxidation for 15 min at 500°C and after approximately 10 days oxidation at 200°C. Neglecting B and C within the oxide scale and assuming ideal orthorhombic MoO₃ on top of Mo₂BC coating the Pilling-Bedworth Ratio R_{PB} [96] can be used to estimate whether the oxide scale is protective or not. Based on the reported molar volume of MoO₃ of 30.7 cm³/mol [97] and a calculated molar volume of Mo₂BC of 24.58 cm³/mol a R_{PB} of 2.5 was calculated with Equation 21 where V_{ox} and V_{M} are the molar volumes of the oxide and compound and v_{M} is the stoichiometry of the Metal in the oxidation reaction (0.5 for Mo₂BC).

$$R_{PB} = \frac{V_{ox}}{v_c V_c} \tag{21}$$

For the calculation of the molar volume of Mo_2BC the density of 8.74 g/cm³ [98] and masses of 95.96 ,10.91 and 12.011 amu [9] for Mo, B and C, respectively, were used. The calculated R_{PB} of 2.5 is associated with adhesive failure of the oxide scale, and hence no protection of MoO_3 can be expected. However, within this report no evidence for adhesive (or cohesive) failure could be observed.

Based on the data discussed no protective oxide formation was observed for Mo_2BC thin films. While oxidation for up to 7 days at $200^{\circ}C$, corresponding to approximate temperatures in particleboard machining [22], amorphous oxide scale formation following a scale thickness kinetics with a power law of n = 0.63 was observed. For oxidation longer than 7 days a significant increase in oxidation kinetics was observed and associated with

crystallization of the initially amorphous oxide scale. While oxidation at 100°C, corresponding to approximate temperatures during solid wood machining [22], the oxide scale thickness of 22 nm ± 10 nm corresponds to only 5% of the oxide scale thickness of 401 nm ± 33 nm observed for 200°C. Based on the findings reported in this study, the application of Mo₂BC as protective coating is limited to processes with temperatures close to 100°C or below. In addition to wear resistant decorative coating applications, the reported steady-state tool surface temperatures of 127°C in solid wood machining and the necessity to protect the utilized cemented tungsten carbide tools from wear [22], suggests that Mo₂BC with its unique property combination of high stiffness, hardness and moderate ductility [10, 85, 86] would be an ideal candidate coating material.

4.4 Summary

The low temperature oxidation behavior of Mo₂BC coatings was investigated systematically for various temperatures ranging from 500 to 100°C for up to 28 days. The onset of oxidation was identified after oxidation for 15 min at 300°C based on a significant increase of surface oxygen content from 3 at. % in the as deposited state to 14 at.%. Oxide scales containing crystalline MoO₃ were obtained after oxidation for 15 min at 500°C and 10 days at 200°C. The oxide scale thickness measured after 14 days at 100°C is 22 nm ± 10 nm which is significantly lower than after 14 days at 200°C with 401 nm ± 33 nm. Furthermore, after 28 days oxidation at 100°C the oxide scale thickness is with 13 nm ± 3 nm comparable to oxidation data at 100°C for 14 days. The reported oxidation behavior qualifies Mo₂BC for application at temperatures close to 100°C or below.

5 Synthesis and properties of orthorhombic MoAIB coatings

5.1 Introduction

The synthesis of orthorhombic bulk MoAIB was reported by Rieger et al. in 1965 [25]. Kota et al. studied the oxidation behavior of bulk MoAlB produced by hot pressing from MoB and Al powders at 1200°C for 5h [24]. Xu et al. studied the oxidation behavior of bulk MoAIB synthesized in a three-step process of MoAIB powder synthesis at 1100°C, etching of surplus AI, followed by hot pressing at 1600°C to increase the density. It is shown that a dense, protective and adherent alumina scale is formed on bulk MoAIB after cyclic oxidation at 1600°C for a total of 50 hours [30]. Shi et al. oxidized needle shaped and plate like MoAlB single crystals and infer from the difference in average weight loss that the oxidation behavior is anisotropic [99]. While the application at high temperatures of most transition metal borides is hampered by their limited oxidation resistance above 1200°C [26, 27], MoAIB forms a protective Al₂O₃ layer [24], was reported to be capable of selfhealing [28] and hence, holds great promise as high temperature material [24, 28, 29, 30]. Here, we report the synthesis of orthorhombic MoAIB coatings for the first time and compare the oxidation behavior at 1200°C to literature reports for bulk material [28, 29] and Ti₂AIC [32, 33].

5.2 Materials and Methods

5.2.1 Experimental Methods

MoAIB coatings were synthesized by combinatorial DC magnetron sputtering [100] using a two target setup. The depositions were carried out in a lab-scale sputtering system [101]. A compound MoB (2" diameter, Plansee Composite Materials GmbH, Lechbruck am See, Germany) and an elemental Al (2" diameter, 99.99% purity) target were placed

each at a 45° angle with respect to the substrate normal. This geometric arrangement enables the deposition of Mo-Al-B coatings with an Al concentration gradient, commonly referred to as composition spread. The target-to-substrate distance was 10 cm. One side-polished Al₂O₃ (0001) single crystal wafers with a diameter of 2" were used as substrates. Prior deposition onto the polished substrate surface, the unpolished sapphire wafer side was covered with approximately 300 nm of Mo to enable efficient heat absorption from the heater positioned behind the substrate. The magnetrons were powered by MDX 2.5 kW (Advanced Energy, USA) and Maris GS 15 (ADL, Darmstadt, Germany) generators, supplying power densities of 6.1 and 1.5 W/cm² to the MoB and Al targets, respectively. The base pressure at the deposition temperature of 700°C was < 1.1x10⁻⁴ Pa. Sputtering was conducted at an Ar (99.999% purity) pressure of 0.35 Pa. The deposition time was 2h and the coating thickness for the close to stoichiometric composition was 1.86 ± 0.05 μm. Hence, the deposition rate for the close to stoichiometric composition was 0.93 μm/h.

Phase formation was investigated with a Bruker D8 Discovery general area detector diffraction system (GADDS) (Bruker, Billerica, MA, USA) using Cu(Kα) radiation with a grazing incident angle of 10°.

Nanoindentation was performed with a Hysitron TI-900 TriboIndenter[™] (Bruker, Eden Prairie, MN, USA). Young's modulus and hardness values were obtained by the method of Oliver and Pharr.[39] Load-controlled measurements were carried out with a maximum load of 10 mN, resulting in an average contact depth of 157 nm (< 10% of coating thickness). A diamond Berkovich tip (~100 nm radius) was used and 100 load displacement data sets were utilized to calculate the average elastic modulus from the

indentation modulus utilizing the Poisson's ratio of $\nu = 0.23$ which was obtained by *ab* initio calculations.

The chemical composition of the combinatorial coating was measured by energy dispersive X-ray spectroscopy (EDX) attached to a JEOL JSM-6480 scanning electron microscope (SEM) (JEOL Ltd., Tokyo, Japan) operated at an acceleration voltage of 5 kV. A calibration sample for EDX was quantified by time-of-flight elastic recoil detection analysis (ToF-ERDA), details can be found in work of Gleich *et al.* [102]. The coating with close to stoichiometric composition (Figure 19(b)) was measured 6 times to determine the statistical uncertainty of EDX to be 4% relative. The statistical uncertainty of the ERDA analysis was < 0.5% absolute. Due to the uncertainty of the specific energy loss of the probing ions and the constituents and of the target, a systematic uncertainty of 5 to 10% relative of the values for the deduced concentrations was assumed. Thus, the concentrations obtained from ERDA-calibrated EDX measurements are calculated to be subject of cumulative measurement uncertainties between 6 and 11% relative deviation.

Thin lamellae (< 100 nm thickness) of the MoAlB coatings in the as deposited state as well as after oxidation for 30 minutes at 1200°C in ambient air were prepared by focused ion beam (FIB) utilizing a FEI Helios Nanolab 660 dual-beam microscope. Subsequently, the cross-section morphology was investigated utilizing a JEOL JSM-2100 transmission electron microscope (TEM) in scanning mode (STEM) with an acceleration voltage of 200kV. In addition, a lamella from the MoAlB coating with close to stoichiometric composition was analyzed in detail by several TEM methods such as high resolution TEM (HRTEM), high-angle annular dark field (HAADF) imaging in STEM, selected area electron diffraction (SAED), EDX, and electron energy loss spectroscopy (EELS). The HRTEM was performed using a FEI spherical aberration (Cs) image corrected Titan

Themis at an acceleration voltage of 300 kV. Both STEM-EELS and STEM-EDX mapping were conducted with a FEI Titan Themis equipped with Cs probe corrector and high-energy resolution Gatan image filter (Quantum) operating at 300 keV acceleration voltage. Compositional area fractions were quantified from EDX spectra utilizing the MATLAB code presented in the work of Zhang *et al.*[103] Core loss STEM-EELS spectra were acquired at 1 eV energy resolution measured from the full width of half maxima of the zero loss peak. The spectra were collected with a 5 nm aperture at an energy dispersion of 0.10 eV per Channel.

5.2.2 Theoretical Methods

Density functional theory (DFT) [104] calculations implemented within the Vienna *ab initio* simulation package (VASP) [76, 77] were performed to calculate the elastic moduli of MoAlB. Generalized gradient approximation (GGA) parametrized by Perdew, Burke and Ernzerhof (PBE) [78] was used with projector augmented wave potentials [79]. Reciprocal space integration using the Monkhorst-Pack scheme [81] as well as the tetrahedron method for total energy using Blöchl-corrections [80] were employed for the calculations. The used *k*-point grid was 8x8x8 for a unit cell containing a total of 12 atoms. Electronic relaxation convergence and energy cut-off were 0.01 meV and 500 eV, respectively. For the determination of elastic constants the formalism described by Ravindran *et al.* [43] was used. Approximations of Reuss [45], Voigt [44] and Hill [46] were applied to estimate the shear modulus *G* and bulk modulus *B*. The Young's modulus *E* is calculated from Equation (22).

$$E = (9BG)/(3B+G), (22)$$

5.3 Results and Discussion

Structural and compositional data obtained along the AI concentration gradient of the composition spread in the MoAIB coating are presented in Figure 19 and Table 2, respectively. The diffraction data (Figure 19(a)) determined for the Al-rich coating with Mo/AI = 0.73 and Mo/B = 1.04 is consistent with a phase mixture of orthorhombic MoAIB and hexagonal AlB₂. All diffraction data determined for the coating with close to stoichiometric composition of Mo/AI = 0.93 and Mo/B = 0.87 provide evidence for the formation of phase pure orthorhombic MoAlB (Figure 19(b)). The diffraction data for the Aldeficient coatings with Mo/AI = 1.38 and Mo/B = 0.83 can be attributed to the formation of hexagonal α-MoB₂ in addition to the MoAlB phase (Figure 19(c)). It may be speculated that the changes in preferred orientation observed along the Al concentration gradient are at least in part caused by changes in chemical composition as well as by the formation of secondary phases. Annealing the close to stoichiometric MoAlB coating at 1200°C for 30 minutes in ambient air resulted in the formation of α-Al₂O₃ and rhombohedral Mo₂B₅ phases (Figure 19(d)). The Al-rich coating is the only one where the MoAlB basal plane peak (020) at 12.7° can be identified. In all other coatings the basal plane peak intensity is very low. The oxygen content of all as deposited samples is ≤ 6 at.% and may originate from impurities within the target, residual gases in the process chamber [105] and subsequent oxidation due to atmosphere exposure [106].

The MoAIB coating synthesis temperature of 700°C reported here, is 500°C lower as the temperature utilized during reactive hot pressing of bulk MoAIB [24]. It is reasonable to assume that the significant decrease in synthesis temperature is enabled by surface diffusion during vapor phase condensation similarly to Mo₂BC [49] and Cr₂AIC [107].

HRTEM images of the close to stoichiometric coatings in Figure 20(a) provide interplanar spacing indicating the formation of MoAlB. No evidence for the formation of impurity phases was obtained. Two different grains are examined along [001] (Figure 20(a)-(b)) and [010] (Figure 20(c)). The lattice spacing of the (020) plane is 6.98 Å, corresponding to a $\bf b$ lattice vector of 13.96 Å \pm 0.26 Å (see Table 3). From Figure 20(c) we deduce lattice parameters of $\bf a$ = 3.17 Å \pm 0.16 Å and $\bf c$ = 3.12 Å \pm 0.08 Å. The uncertainties are based on the standard deviation of 20 measurements. Both, the theoretically and the experimentally determined lattice parameters deviate by < 1.6% with respect to each other and to previous reports (see Table 3). Considering the employed exchange-correlation functionals within DFT a relative error of \leq 2% has to be expected for lattice constants.[108] Hence the here reported theoretical and experimental data are in excellent agreement with each other as well as with previous reports [24, 109].

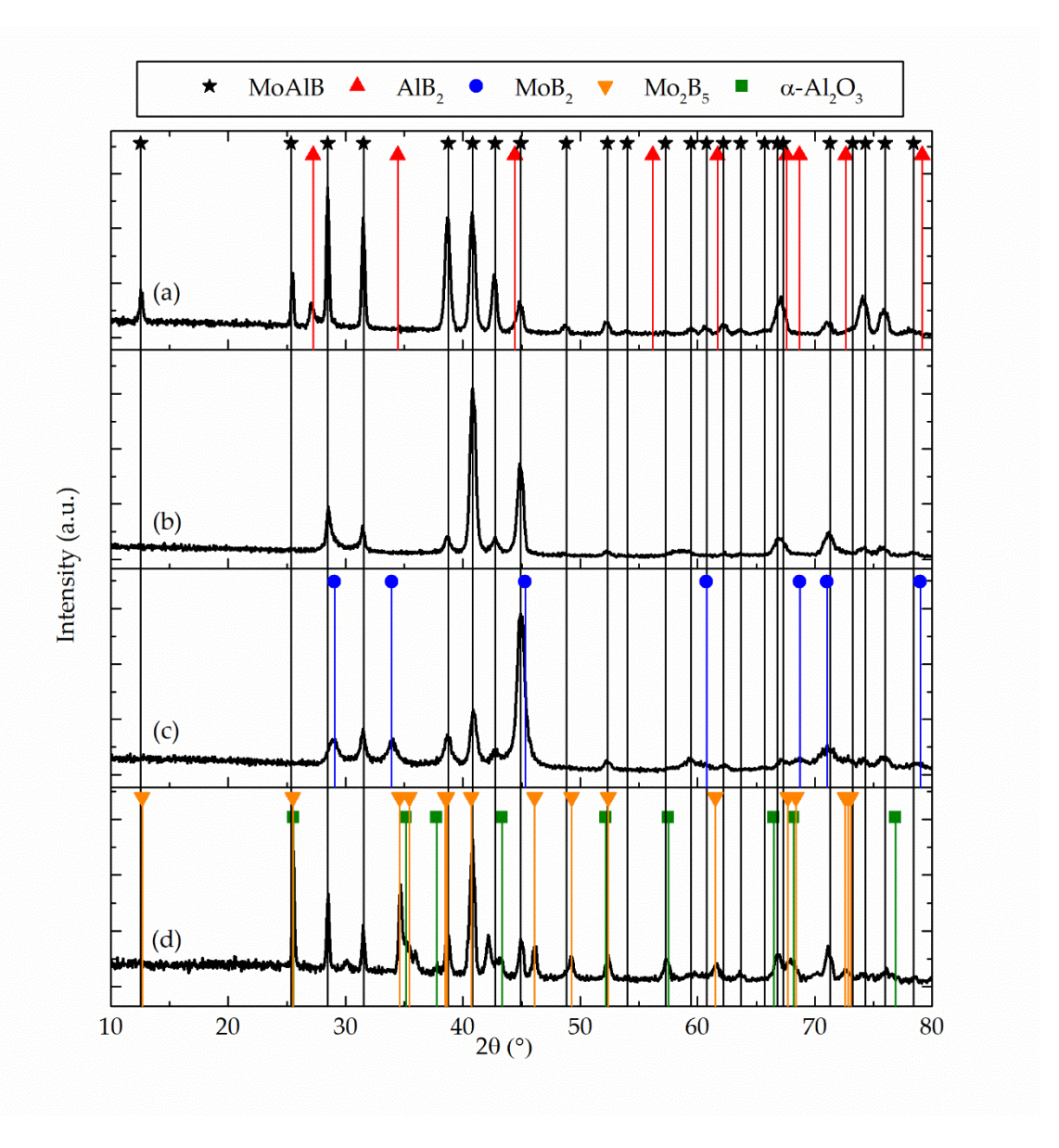


Figure 19. X-ray diffraction data of Al-rich MoAlB (a), close to stoichiometric MoAlB (b) and Al-deficient MoAlB (c) deposited at 700°C substrate temperature. Close to stoichiometric MoAlB annealed at 1200°C for 30 minutes in ambient air is shown in (d). For all compositions the orthorhombic MoAlB crystal structure is the dominant phase.

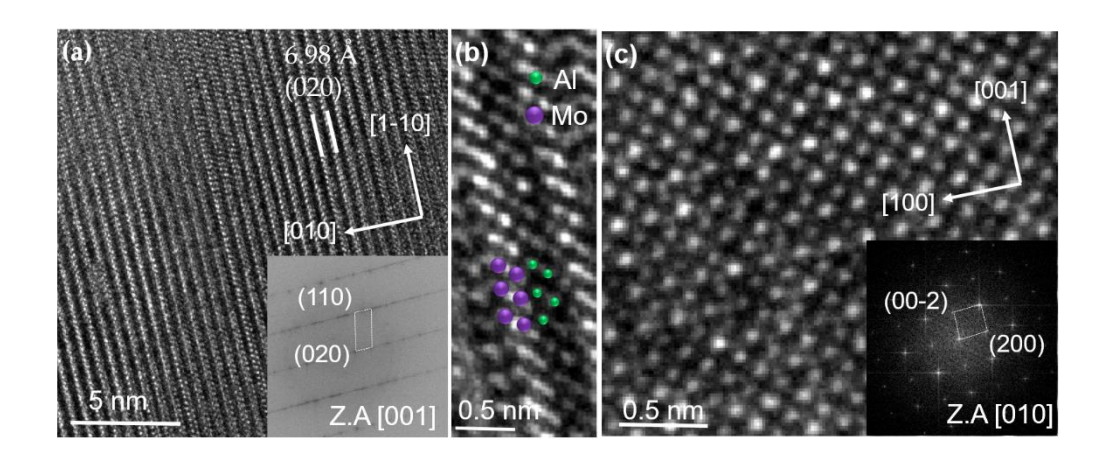


Figure 20. HRTEM images of the close to stoichiometric coatings from (a) and (b) show the atomic arrangement of Mo and Al along [001] zone axis and (c) along [010] zone axis. Purple and green symbols represent positions of Mo and Al in Figure 20(b). The insets present the corresponding fast Fourier transform (FFT).

Table 2. Compositional data of as deposited coatings

Coating	Mo (at.%)	Al (at.%)	B (at.%)	O (at.%)
Al-rich	28.9±3.2	39.4±4.3	28±3	4±1
close to stoichiometric	29.4±3.2	31.5±3.5	34±4	5±1
Al-deficient	32.0±3.5	23.2±2.6	39±4	6±1

Table 3. Experimental and theoretical lattice parameters of MoAIB compared to literature data.

a (Å)	b (Å)	c (Å)	Ref.
3.24 ± 0.04	13.95 ± 0.72	3.10 ± 0.08	XRD
3.17 ± 0.16	13.96 ± 0.26	3.12 ± 0.08	HRTEM/SAED
3.223	14.016	3.110	DFT
3.21	13.98	3.10	[24]
3.2227	14.037	3.1067	[109]

STEM-EDX (Figure 21(b)-(d)) and STEM-EELS (Figure 21(f)) measurements were performed to qualitatively analyze the local elemental composition of the MoAlB coating with a close to stoichiometric integral composition. Darker regions in the HAADF STEM image depicting the as deposited state may be caused by local enrichment of light elements, such as oxygen, and/or by the presence of pores. The EELS data, averaged over the identical region as mapped by EDX, show the element specific Al L_{2,3} (73.5 eV),

Al L₁(119.4 eV), and B K (192.2 eV) edges. The observed reflections in the SAED pattern (Figure 21(e)) confirm the formation of orthorhombic MoAlB consistent with XRD. However, additional reflections, indicated by black arrows, are attributed to a yet unidentified impurity phase. Principle component analysis (PCA) of the EDX map using the code described in [103] revealed the presence of two impurity phases besides the main MoAlB phase: An Al-rich and O-rich phase. The obtained weight maps for Al and O are displayed in Figure 22. The maps were subsequently used to calculate the areal fraction of the Al-rich and O-rich impurity phases and found to be on the order of 4% and 5 to 6%, respectively.

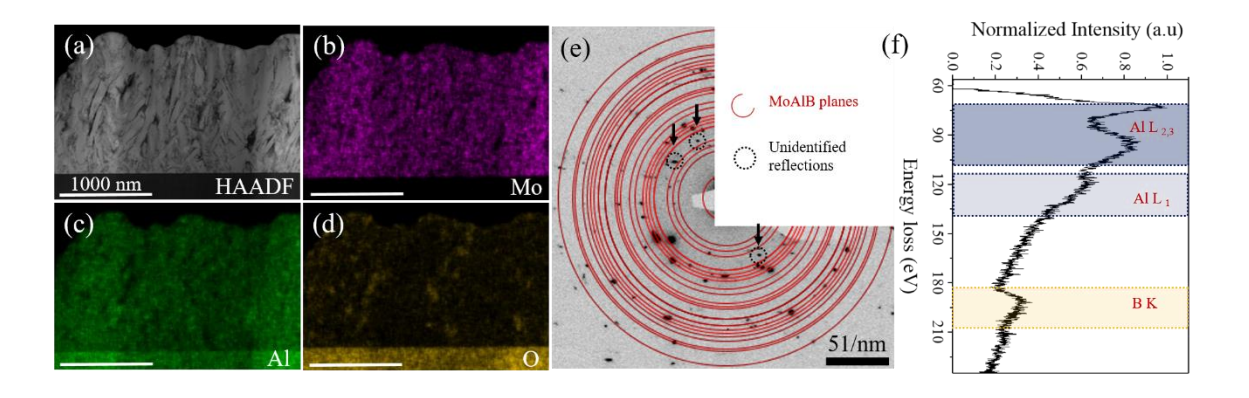


Figure 21. HAADF STEM image of a cross-section obtained from the close-to-stoichiometric coating (a). (b) to (d) show STEM-EDX maps for Mo, AI, and O, respectively. Reflections in SAED pattern (e) indicate the formation of orthorhombic MoAIB. Unidentified reflections are marked with black arrows. (f) shows the EELS data in the energy loss region of the AI L, and B K edges.

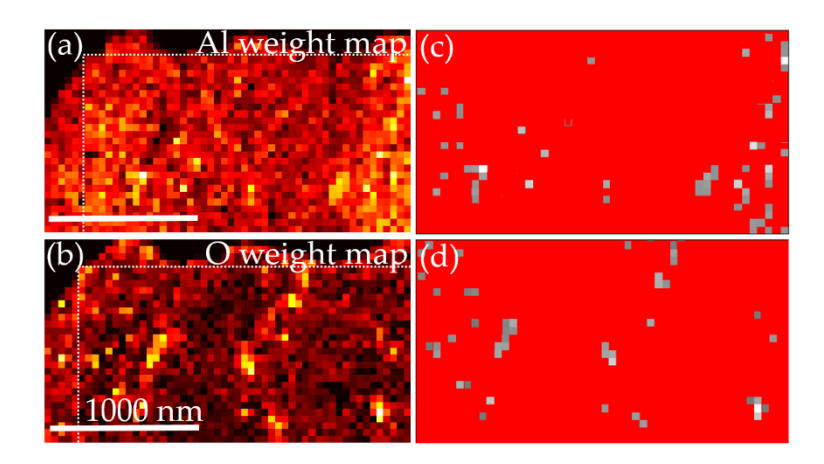


Figure 22. (a) and (b) depict the EDX weight mappings processed with the MATLAB Code from Zhang *et al.*[103] for Al (a) and O (b). Area fraction (grey regions) of Al-rich (c) and O-rich (d) impurity phases analyzed utilizing ImageJ. The areal fraction for the Al-rich and O-rich phase are 4% and 5 to 6%, respectively.

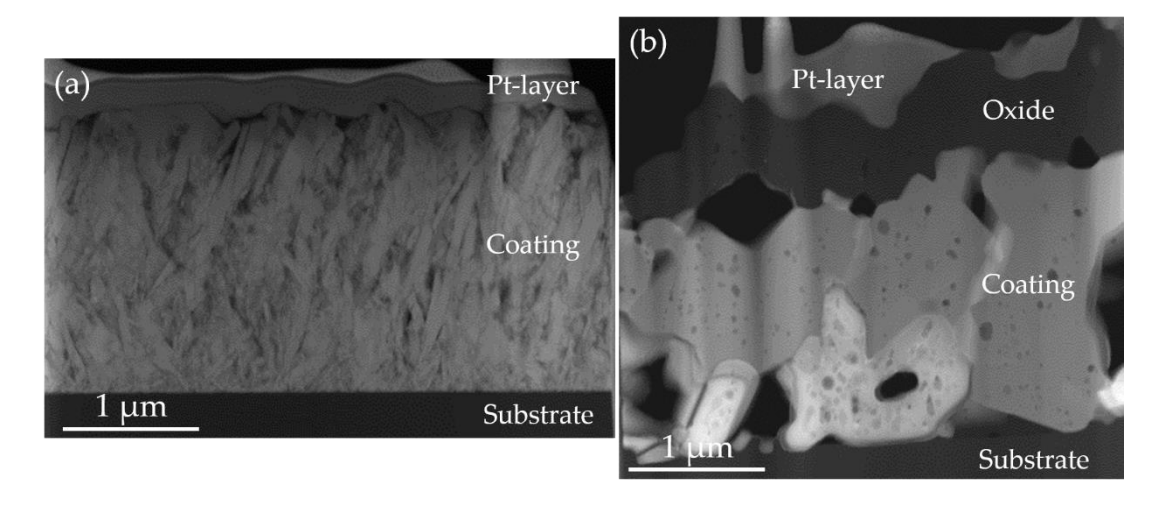


Figure 23. STEM of close-to-stoichiometric MoAlB coating. (a) as deposited, (b) after oxidation in ambient air for 1200°C. The top layer corresponds to the Pt protection layer which is deposited during FIB sample preparation.

STEM cross-sectional images of the close-to-stoichiometric MoAIB coating before and after oxidation are shown in Figure 23. In the as-deposited state the coating thickness is $1.86 \pm 0.05 \, \mu m$ compared to a total coating thickness after annealing of $2.19 \pm 0.14 \, \mu m$ consisting of coating and oxide scale. Pores with diameter of up to 500 nm form in the oxidized coating. Pore formation during oxidation of bulk MoAIB was previously observed

by Kota et al. [29] and Lu et al. [28] and was attributed to the evaporation of volatile MoO3 and B₂O₃ [28]. Oxide scale growth of 0.59 ± 0.12 µm in 30 minutes was observed for the MoAIB coating annealed at 1200° for 30 minutes. (Figure 23(b)-(c)). According to Kota et al. the mass gain oxidation kinetics of bulk MoAIB at 1200°C is closer to linear than to parabolic or cubic [29]. However, if the scale thickness is considered, the best fits to the measured data are given by cubic and parabolic kinetics with correlation coefficients of 0.972 and 0.967, respectively. For bulk MoAIB a scale thickness at identical oxidation conditions of 1.42 μ m \pm 0.57 μ m and 0.52 μ m \pm 0.21 μ m can be calculated using the rate constants reported by Kota et al. [29] of 1.60 x 10⁻²¹ m³s⁻¹ and 1.49 x 10⁻¹⁶ m²s⁻¹ for cubic and parabolic kinetics, respectively. It has to be kept in mind that these thickness values are computed from kinetics data for which the shortest oxidation time was 5 hours. The thickness error given above is estimated assuming the same relative uncertainty than reported for the 5 hours oxidation data, namely ±40%. Recently, Lu et al. [28] investigated the oxidation of bulk MoAIB at 1200°C for up to 10 hours and reported thickness measurements of the oxide scale in two hour intervals. They reported parabolic scale thickening kinetics. Also from these investigations we have extrapolated the scale thickness to be expected at 30 minutes oxidation time and obtained 0.6 ± 0.05 µm which is in excellent agreement with the here measured scale thickness formed on the MoAlB coating, see Figure 24. As no rate constant was reported by Lu et al. the data reported in Figure 1 of reference 5 was utilized for the aforementioned extrapolation. Similarly, to the extrapolation discussed above also here it has to be kept in mind that the thickness value is extrapolated from thickness data for which the shortest oxidation time was 2 hours and that the thickness error given is estimated assuming the same relative uncertainty than reported for the 2 hours oxidation namely ±8%. In Figure 24 the here measured data is compared with extrapolated literature data of the oxide scale growth of bulk MoAIB [28, 29] it is evident that the MoAIB coating (black) exhibits similar oxidation behavior as bulk MoAIB.

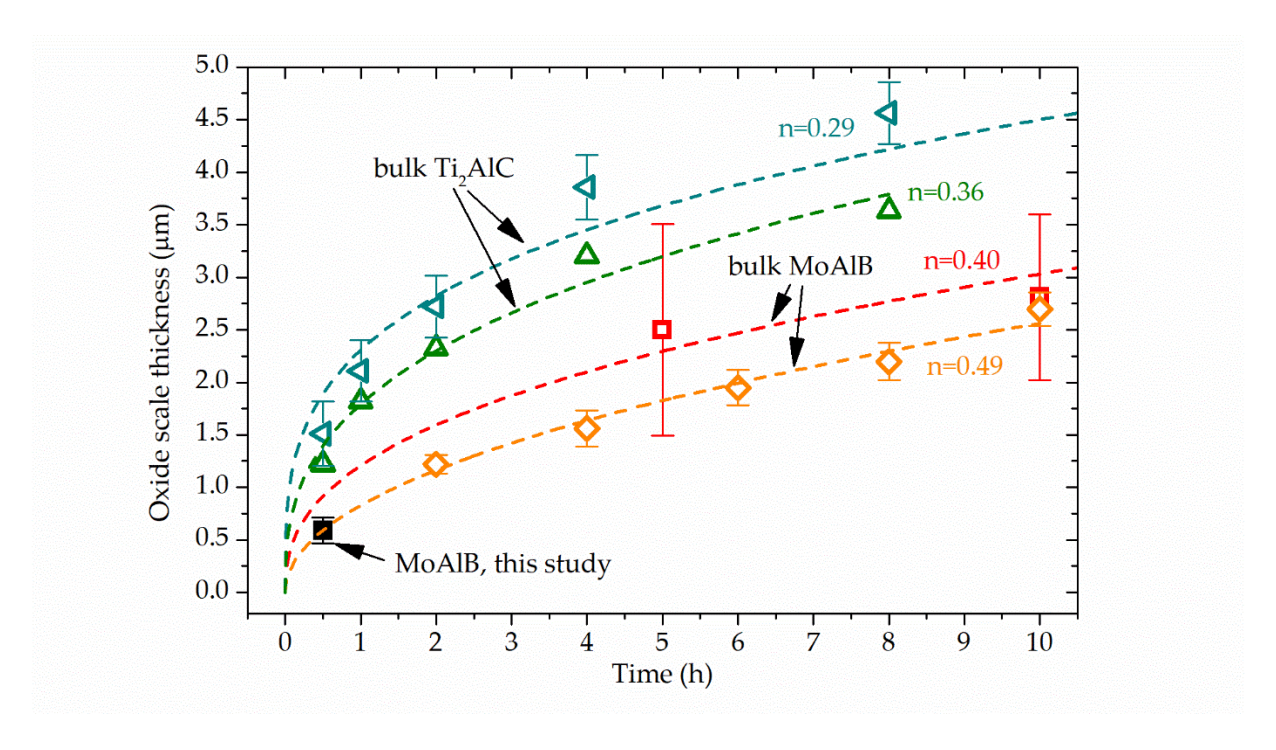


Figure 24: Comparison of oxide scale thickness formed at 1200° C in air of the here investigated MoAlB coating with bulk MoAlB and bulk Ti₂AlC. The bulk Ti₂AlC data are plotted in dark teal left hand triangle [33] and green triangle [32] while the bulk MoAlB data are plotted in red square [29] and orange inclined square [28]. For the oxidation behavior of bulk MoAlB the reported power factors of n = 0.40 [29] and n = 0.49 [28] were utilized to compute the dashed lines for red square and orange inclined square, respectively. For the Ti₂AlC data reported in references [33] and [32] the power factors were calculated according Equation 23. The calculated power factors n are given.

As the similarity notion above is based on an extrapolation rather than on a direct comparison with oxide thickness data, the oxidation behavior of the MoAlB coating is also compared to that of alumina forming bulk Ti₂AlC [32, 33]. This comparison is shown in Figure 24. The power factor n for the Ti₂AlC data from references 9 and 32 were calculated

with Equation 23, where d is the oxide scale thickness, K the rate law constant and t the oxidation time.

$$d = Kt^n, (23)$$

The reported oxide scale thickness formed on bulk Ti₂AlC when oxidized in dry air at 1200° C for 30 minutes are $1.50 \pm 0.30 \ \mu m$ [33] and $1.22 \pm 0.05 \ \mu m$ [32] and are hence at least twice as large as the here reported scale thickness on the MoAlB coating at identical oxidation temperature and duration. After 8 hours at 1200° C the reported scale thicknesses on bulk Ti₂AlC are with $3.63 \pm 0.08 \ \mu m$ [32] and $4.56 \pm 0.29 \ \mu m$ [33] also significantly larger as the reported bulk MoAlB scale thickness of $2.20 \pm 0.18 \ \mu m$ [28].

Hence, as the here reported MoAIB coating exhibits less than half of the oxide scale thickness as bulk Ti₂AIC after 30 minutes oxidation at 1200°C. This mirrors the oxidation behavior comparison between bulk MoAIB [28] and bulk Ti₂AIC [32, 33], where significantly larger oxide scale thicknesses are observed for Ti₂AIC, see Figure 24.

The theoretically determined Young's modulus of 359 GPa is well within the error margin of the Young's modulus determined by nanoindentation of 349 \pm 57 GPa. The scattering of experimental data of \pm 16 % is most likely caused by the surface roughness of R_a = 44 nm determined by laser optical microscopy. The relative error of elastic properties determined by DFT of \leq 20% for the employed exchange-correlation functionals has to be expected [108]. Theoretically predicted and experimentally determined moduli of G_{DFT} = 145 GPa, E_{DFT} = 359 GPa, B_{DFT} = 225 GPa and E_{exp} = 349 \pm 57 GPa from this work deviate by < 7 % compared with moduli determined by resonant ultrasound spectroscopy of G = 151.2 GPa, E = 372.9 GPa and E = 232.9 GPa at 300 K [110], and hence are in excellent agreement. The determined hardness value of 13 \pm 3 GPa is

comparable to reported hardness values of 10.3 ± 0.2 GPa [24] and 11.4 to 13.6 GPa [111] determined for bulk MoAIB and single crystal MoAIB, respectively. It is reasonable to assume that this hardness increase may be caused by orders of magnitude smaller grain sizes in coatings (typically < 100 nm) compared to bulk materials (typically > 1 μ m). The calculated B/G ratio [15] and Cauchy pressure [16] of MoAIB predict brittle behavior and are comparable to hard coatings such as TiN and TiAIN as shown in Table 4.

Table 4. B/G ratio, Cauchy pressures for (100), (010) and (001) planes

Material	$\frac{B}{G}$	С ₂₃ — С ₄₄ (GPa)	С ₁₃ — С ₅₅ (GPa)	С ₁₂ — С ₆₆ (GPa)	Ref
MoAIB	1.55	-61	10	-20	This study
Mo ₂ BC	1.73	27	-31	31	[17]
TiN	1.58	-21	-21	-21	[112]
VAIN	1.40				[113]
TiAIN	1.42	-45	-45	-45	[114]

5.4 Summary

We report the first synthesis of X-ray phase pure orthorhombic MoAlB coatings at 700°C. The oxidation kinetics of MoAlB coatings at 1200°C in ambient air are comparable to bulk MoAlB samples. Hence, MoAlB coatings exhibit significantly lower oxidation kinetics than bulk Ti₂AlC. Finally, measured elastic properties of MoAlB coatings are in excellent agreement with *ab initio* predictions. The ductility criteria B/G ratio and Cauchy pressure are comparable to hard coatings, such as TiN and TiAlN.

6 Conclusions

The synthesis, characterization and oxidation behavior of Mo₂BC and MoAlB thin films were investigated by combining *ab initio* calculations, Monte Carlo simulations, coating synthesis by direct current magnetron sputtering and a large variety of characterization methods. Based on the combination of experimental and theoretical approaches the following contributions to knowledge were made:

I) The evolution of the angle-resolved composition of Mo-B-C thin films deposited from a Mo2BC compound target was investigated experimentally and theoretically as a function of the Ar and Kr pressure. Samples were positioned in a specific angular arrangement from $\alpha = 0^{\circ}$ to $\pm 67.5^{\circ}$ with respect to the target normal with a fixed target substrate distance. Considering the simulated mass-dependent initial angular distribution functions, a convex distribution for Mo was observed, whereas B and C, exhibit concave distributions as consequence of reflective collisions in the collision cascade. B and C can only be backscattered by the heavy Mo leading to the preferential ejection of B and C close to the target normal. Obviously, Mo cannot be backscattered due to a reflective collision with a lighter element. Within experiments and simulations, the observed change in angle-resolved composition as result of a by one order of magnitude increased Ar pressure was lower than the expected measurement error and hence, cannot be resolved by EDX. Contrary, sputtering by Kr+ results in significantly larger deviations between the target and the film composition. These deviations can be rationalized based on reflective collisions in the collision cascade. As the Kr pressure is increased scattering during transport in the gas phase results in angle resolved compositions that approach the target composition. Furthermore, based on considering the relative contributions of the number of collisions and scatter angle to the average trajectory length it is inferred that the significantly larger average trajectory length of Mo in Kr compared to Ar can be rationalized by an on average larger scattering angle of Mo. It is shown that the mass ratio between sputtering gas and sputtered species defines the scattering angle within the collision cascades in the target as well as for the collisions in the gas phase, which in turn define the angle- and pressure-dependent film compositions.

- II) Mo₂BC coatings exhibit a unique combination of high stiffness and moderate ductility, which is ideally suited for protective applications. However, the low temperature oxidation behavior of these coatings has not been investigated systematically yet. Here, Mo₂BC coatings, synthesized by direct current magnetron sputtering, were oxidized at temperatures as low as 100°C for up to 28 days. Based on Time-of-Flight elastic recoil detection analysis the onset of oxidation of Mo₂BC coatings was found approximately after oxidation for 15 min at 300°C. The formation of crystalline oxide scales was observed after oxidation for 15 min at 500°C and 10 days at 200°C as orthorhombic MoO₃ was identified by X-ray diffraction. Scale thickness measurements by scanning transmission electron microscopy reveal oxide scale thickness values of 401 nm ± 33 nm and 22 nm ± 10 nm after oxidation for 14 days at 200°C and 100°C, respectively. Increasing the oxidation time to 28 days at 100°C an oxide scale thickness of 13 nm ± 3 nm was measured. Hence, based on the combination of mechanical properties and the here reported low temperature oxidation behavior Mo₂BC coatings are proposed as candidate materials for solid wood machining applications as well as low temperature forming operations.
- III) X-ray phase pure, orthorhombic MoAlB coatings were grown at 700°C. High resolution transmission electron microscopy reveals an interplanar spacing which is in

excellent agreement with the lattice parameter determined by X-ray diffraction and *ab initio* predictions as well as literature reports. In selected area electron diffraction and compositional area fraction analysis, additional, yet unidentified, Al-rich and O-rich minority phases were observed. MoAlB coatings exhibit similar oxidation behavior as bulk MoAlB as the oxide scale thickness formed on MoAlB coatings after oxidation at 1200°C for 30 minutes is similar to the one extrapolated for bulk MoAlB. Furthermore, MoAlB coatings exhibit significantly lower oxidation kinetics as bulk Ti2AlC. Measured elastic properties of the as deposited MoAlB coatings are in excellent agreement with *ab initio* predictions and literature values for bulk MoAlB. The calculated B/G ratio and Cauchy pressure are comparable to hard coatings such as TiN and TiAlN.

In summary, it was shown that the deviation between Mo₂BC compound target composition and Mo-B-C thin film composition significantly depends on the mass ratio of sputter gas and sputtered species. Furthermore, the mechanical properties and the here reported low temperature oxidation behavior qualify Mo₂BC as protective coating in solid wood machining and low temperature forming operations. Finally, the first thin film synthesis of MoAlB coatings, which exhibit a similar oxidation behavior as bulk MoAlB, was reported.

7 Future Work

Based on the research conducted in this thesis, several directions for future work are meaningful. It was shown that the scattering angle within the collision cascade in the target as well as the scattering while gas phase transport, which ultimately defines the thin film chemical composition, strongly depends on the mass ratio of sputtering gas and sputtered species. By variations in Kr gas pressure the content of Mo within the thin films could be changed significantly. Based on these findings, the utilization of an even heavier gas, such as Xe with its mass of 131.3 amu [9], should lead to a more effective scattering of Mo, exhibiting a mass of 95.96 amu [9]. This in fact could be used to further decrease the deviation of target and thin film composition. The industrial relevance of this should be critically considered as Xe is significantly more expensive than Ar. From the opposite point of view, one could also utilize a gas which mass is less than the light elements B and C to decrease the effective scattering of light elements and promote the forward flux from the target. This might be challenging as Ne with a mass of 20.18 amu is still significant heavier than B and C. First experiments were conducted with Ne to test this idea but have proven problematic as the ignition of the plasma was not possible with a reasonable target power. This was correlated to the comparable high ionization energy of Ne⁺ of 21.56 eV [115] which is larger than the one for Ar⁺ of 15.75 eV [115] and Kr⁺ of 13.99 eV [116]. Furthermore, the large mass difference of Ne and the heaviest target constituent Mo with masses of 21.18 amu and 95.96 amu [9], respectively, allows low momentum and energy transfer during collisions.

To further validate the findings of the angle resolved investigations, mass energy spectroscopy could be performed to experimentally determine the angular and energy

distribution function of target constituents. A special rotatable magnetron designed by Stanislav Mráz at MCh, RWTH Aachen University, can be used for this approach as the design perfectly fits the experimental setup of this study.

In the second part of this work the low temperature oxidation behavior of Mo₂BC was systematically studied. The findings discussed above limit the application temperatures of Mo₂BC because of its oxidation behavior to 100°C or below, such as solid wood machining. While the unique property combination of high stiffness and moderate ductility promote Mo₂BC to be an ideal candidate as wear resistant coating, an enhanced oxidation resistance would offer a variety of new applications. One way to achieve this would be to alloy Mo₂BC with elements known for their ability to form a protective oxide scale. One example is MoAlB, which is so far the only known oxidation resistant transition metal boride, forming a dense and adherent alumina scale up to 1600°C in ambient air [30], the addition of AI may increase the oxidation resistant of Mo₂BC. For this purpose, the approach of combinatorial magnetron sputtering, leading to a compositional gradient of Al within the Mo₂BC thin film would be helpful for a high throughput investigation. First, ab initio DFT calculations are suggested to predict the solubility of Al in Mo₂BC, potential atomic positions (substitution or interstitial) as well as most important, the impact on elastic properties. An increase in oxidation resistance but a loss of the unique property combination would be a step in the wrong direction.

Furthermore, a potential way to improve the oxidation resistance of Mo₂BC thin films might be the addition of a secondary phase, such as MoAlB. Similarity in crystal structure and atomic order, especially the boron zigzag (see Figure 1) might enable a laminated structure of Mo₂BC – MoAlB.

In the last part of this thesis, the first thin film synthesis of the so far only known oxidation resistant transition metal boride MoAlB is reported. Details of the oxidation mechanism are still unclear and require further studies [29]. To solve this discrepancy, it is proposed to perform short time annealing experiments at 1200°C in a time regime of seconds to investigate the very early stage of oxidation. Reports on this oxidation stage are rare and a systematic study would lead to further understanding of the impact of local segregation during early stage oxidation. The influence of thin film and oxide scale microstructure and the evolution of microstructure while oxidation need further investigation. Before so, additional studies on the impact of process parameter on MoAlB thin film morphology have to be performed as HAADF STEM analysis of the MoAlB sample discussed in this thesis indicate local light element enrichment and/or porosity. Improved homogeneity in the MoAlB thin films, with respect to composition and morphology, would decrease the degrees of freedom while investigating the early stage oxidation behavior.

Furthermore, bulk MoAlB was recently reported to be capable of self-healing, the ability to fill cracks with oxidation products, such as alumina, and recover initial material strength [28]. The self-healing of MoAlB thin films is unknown and hence, needs to be investigated. Based on a limited Al reservoir in thin films, compared to bulk, carbide formation within the Al depleted zone was reported for Cr₂AlC [117]. In this study the formation of Mo₂B₅ after oxidation was observed. The mechanism for the formation is still unknown but might be correlated to Al depletion in the MoAlB matrix as no Mo₂B₅ formation was reported for bulk MoAlB. The early stage oxidation experiments discussed before might be useful to uncover the underlying mechanism.

8 References

- 1. Momma K, Izumi F. VESTA 3 for three-dimensional visualization of crystal, volumetric and morphology data. Journal of Applied Crystallography. 2011;44(6):1272-1276.
- 2. Eklund P, Beckers M, Jansson U, et al. The Mn+ 1AXn phases: Materials science and thin-film processing. Thin Solid Films. 2010;518(8):1851-1878.
- 3. Neidhardt J, Mraz S, Schneider JM, et al. Experiment and simulation of the compositional evolution of Ti-B thin films deposited by sputtering of a compound target. J Appl Phys. 2008 Sep;104(6). doi: 10.1063/1.2978211. PubMed PMID: WOS:000260119300019:
- 4. Mitterer C. Borides in thin film technology. Journal of Solid State Chemistry. 1997 Oct;133(1):279-291. doi: 10.1006/jssc.1997.7456. PubMed PMID: WOS:A1997YG96600054;
- 5. Kunc F, Musil J, Mayrhofer PH, et al. Low-stress superhard Ti-B films prepared by magnetron sputtering. Surface & Coatings Technology. 2003 Sep-Oct;174:744-753. doi: 10.1016/s027-8972(03)00425-0. PubMed PMID: WOS:000185680300132:
- Mraz S, Emmerlich J, Weyand F, et al. Angle-resolved evolution of the composition of Cr-Al-C thin films deposited by sputtering of a compound target. Journal of Physics D: Applied Physics. 2013 Apr;46(13). doi: 10.1088/0022-3727/46/13/135501. PubMed PMID: WOS:000315948500024;
- 7. Rueß H, to Baben M, Mráz S, et al. HPPMS deposition from composite targets: Effect of two orders of magnitude target power density changes on the composition of sputtered Cr-Al-C thin films. Vacuum. 2017;145:285-289.
- 8. Jo YH, Mohanty BC, Yeon DH, et al. Single elementary target-sputtered Cu2ZnSnSe4 thin film solar cells. Solar Energy Materials and Solar Cells. 2015;132:136-141.
- 9. Wieser ME, Berglund M. Atomic weights of the elements 2007 (IUPAC Technical Report). Pure and Applied Chemistry. 2009;81(11):2131-2156.
- Emmerlich J, Music D, Braun M, et al. A proposal for an unusually stiff and moderately ductile hard coating material: Mo₂BC. Journal of Physics D-Applied Physics. 2009 Sep;42(18). doi: 10.1088/0022-3727/42/18/185406. PubMed PMID: WOS:000269557000049;
- 11. Chen K, Zhao L, Rodgers J, et al. Alloying effects on elastic properties of TiN-based nitrides. Journal of Physics D: Applied Physics. 2003;36(21):2725.
- 12. Mayrhofer P, Music D, Schneider J. Influence of the Al distribution on the structure, elastic properties, and phase stability of supersaturated Ti 1– x Al x N. J Appl Phys. 2006;100(9):094906.
- 13. Yao H, Ouyang L, Ching WY. Ab initio calculation of elastic constants of ceramic crystals. Journal of the American Ceramic Society. 2007;90(10):3194-3204.
- 14. Evans A, Hutchinson J. The thermomechanical integrity of thin films and multilayers. Acta Metallurgica et Materialia. 1995;43(7):2507-2530.
- 15. Pugh S. XCII. Relations between the elastic moduli and the plastic properties of polycrystalline pure metals. Philos Mag. 1954;45(367):823-843.
- 16. Pettifor D. Theoretical predictions of structure and related properties of intermetallics. Mater Sci Tech. 1992;8(4):345-349.

- 17. Bolvardi H, Emmerlich J, Baben MT, et al. Systematic study on the electronic structure and mechanical properties of X₂BC (X = Mo, Ti, V, Zr, Nb, Hf, Ta and W). J Phys-Condens Mat. 2013 Jan;25(4).
- 18. Djaziri S, Gleich S, Bolvardi H, et al. Are Mo2BC nanocrystalline coatings damage resistant? Insights from comparative tension experiments. Surf Coat Tech. 2016;289:213-218.
- 19. Hindam H, Whittle D. Microstructure, adhesion and growth kinetics of protective scales on metals and alloys. Oxidation of metals. 1982;18(5-6):245-284.
- 20. Birks N, Meier GH, Pettit FS. Introduction to the high temperature oxidation of metals. Cambridge University Press; 2006.
- 21. Ashby MF, Jones DRH. Engineering Materials 1, 1996. Oxford: Butterworth Heinemann.
- 22. Ratnasingam J, Ma TP, Ramasamy G. Tool temperature and cutting forces during the machining of particleboard and solid wood. Journal of Applied Sciences. 2010;10(22):2881-2886.
- 23. Ratnasingam J, Ma T, Ramasamy G, et al. The wear characteristics of cemented tungsten carbide tools in machining oil palm empty fruit bunch particleboard. J. Journal of Applied Sciences. 2009;9(18):3397-3401.
- 24. Kota S, Zapata-Solvas E, Ly A, et al. Synthesis and characterization of an alumina forming nanolaminated boride: MoAlB. Sci Rep. 2016;6.
- 25. Rieger W, Nowotny H, Benesovsky F. Über einige Komplexboride von Übergangsmetallen. Monatshefte für Chemie/Chemical Monthly. 1965;96(3):844-851.
- 26. Parthasarathy T, Rapp R, Opeka M, et al. A model for the oxidation of ZrB 2, HfB 2 and TiB 2. Acta Mater. 2007;55(17):5999-6010.
- 27. Fahrenholtz W, Hilmas G. Oxidation of ultra-high temperature transition metal diboride ceramics. International Materials Reviews. 2012;57(1):61-72.
- 28. Lu X, Li S, Zhang W, et al. Crack healing behavior of a MAB phase: MoAlB. Journal of the European Ceramic Society. 2019.
- 29. Kota S, Zapata-Solvas E, Chen Y, et al. Isothermal and Cyclic Oxidation of MoAlB in Air from 1100° C to 1400° C. J Electrochem Soc. 2017;164(13):C930-C938.
- 30. Xu L, Shi O, Liu C, et al. Synthesis, microstructure and properties of MoAlB ceramics. Ceramics International. 2018;44(11):13396-13401.
- 31. Dobrovinskaya ER, Lytvynov LA, Pishchik V. Sapphire: material, manufacturing, applications. Springer Science & Business Media; 2009.
- 32. Li S, Song G, Kwakernaak K, et al. Multiple crack healing of a Ti2AlC ceramic. Journal of the European Ceramic Society. 2012;32(8):1813-1820.
- 33. Song G, Schnabel V, Kwakernaak C, et al. High temperature oxidation behaviour of Ti2AlC ceramic at 1200 C. Materials at High Temperatures. 2012;29(3):205-209.
- 34. Sigmund. Sputtering by Particle Bombardment I edited by Behrisch R. Springer-Verlag; 1981. (Behrisch R, editor.).
- 35. Olson RR, King ME, Wehner GK. Mass effects on angular distribution of sputtered atoms. J Appl Phys. 1979;50(5):3677-3683. doi: 10.1063/1.326321. PubMed PMID: WOS:A1979GZ30100108;
- 36. Friedbacher G, Bubert H. Surface and Thin Film Analysis: A Compendium of Principles, Instrumentation, and Applications. John Wiley & Sons; 2011.

- 37. Goldstein JI, Newbury DE, Michael JR, et al. Scanning electron microscopy and X-ray microanalysis. Springer; 2003.
- 38. Waseda Y, Matsubara E, Shinoda K. X-ray diffraction crystallography: introduction, examples and solved problems. Springer Science & Business Media; 2011.
- 39. Oliver WC, Pharr GM. An improved technique for determining hardness and elastic modulus using load and displacement sensing indentation experiments. J Mater Res. 1992;7(6):1564-1583.
- 40. Fisher-Cripps AC. The IBIS handbook of nanoindentation Fisher-Cripps Laboratories Pty. Limited: NSW; 2009. p. 8-11.
- 41. Birch F. Finite elastic strain of cubic crystals. Phys Rev. 1947;71(11):809.
- 42. Birch F. Finite strain isotherm and velocities for single-crystal and polycrystalline NaCl at high pressures and 300 K. Journal of Geophysical Research: Solid Earth. 1978;83(B3):1257-1268.
- 43. Ravindran P, Fast L, Korzhavyi PA, et al. Density functional theory for calculation of elastic properties of orthorhombic crystals: application to TiSi 2. J Appl Phys. 1998;84(9):4891-4904.
- 44. Voigt W. Lehrbuch der Kristallphysik (Teubner, Leipzig, 1928). 1908:716.
- 45. Reuss A. Berechnung der Fließgrenze von Mischkristallen auf Grund der Plastizitätsbedingung für Einkristalle. ZAMM-Journal of Applied Mathematics and Mechanics/Zeitschrift für Angewandte Mathematik und Mechanik. 1929;9(1):49-58.
- 46. Hill R. The elastic behaviour of a crystalline aggregate. P Phys Soc A. 1952;65(5):349.
- 47. Bovin JO, Okeeffe M, Stenberg L. Planar defects in Mo2BC. An electron microscope study. Journal of Solid State Chemistry. 1977;22(2):221-231. doi: 10.1016/0022-4596(77)90041-x. PubMed PMID: WOS:A1977DY48500017;
- 48. Jeitschko W, Benesovsky F, Nowotny H. Die Kristallstruktur von Mo₂BC. Monatshefte Fur Chemie. 1963;94(3):565-&. doi: 10.1007/bf00903497. PubMed PMID: WOS:A19638382B00006;
- 49. Bolvardi H, Emmerlich J, Mraz S, et al. Low temperature synthesis of Mo2BC thin films. Thin Solid Films. 2013 Sep;542:5-7.
- 50. Sarakinos K, Alami J, Konstantinidis S. High power pulsed magnetron sputtering: A review on scientific and engineering state of the art. Surf Coat Tech. 2010;204(11):1661-1684.
- 51. Ohring. The Materials Science of Thin Films. Academic Press Limited; 1992.
- 52. Emmerlich J, Hogberg H, Sasvari S, et al. Growth of Ti₃SiC₂ thin films by elemental target magnetron sputtering. J Appl Phys. 2004 Nov;96(9):4817-4826. doi: 10.1063/1.1790571. PubMed PMID: WOS:000224799300016;
- 53. Eklund P, Joelsson T, Ljungcrantz H, et al. Microstructure and electrical properties of Ti-Si-C-Ag nanocomposite thin films. Surface & Coatings Technology. 2007 Apr 2;201(14):6465-6469. doi: 10.1016/j.surfcoat.2006.12.016. PubMed PMID: WOS:000245065200039;
- 54. Chen L, Holec D, Du Y, et al. Influence of Zr on structure, mechanical and thermal properties of Ti–Al–N. Thin Solid Films. 2011;519(16):5503-5510.
- 55. Shaginyan LR, Misina M, Kadlec S, et al. Mechanism of the film composition formation during magnetron sputtering of WTi. Journal of Vacuum Science & Technology a-Vacuum Surfaces and Films. 2001 Sep-Oct;19(5):2554-2566. doi: 10.1116/1.1392401. PubMed PMID: WOS:000171376700077;

- 56. Jonsson LB, Hedlund C, Katardjiev IV, et al. Compositional variations of sputter deposited Ti/W barrier layers on substrates with pronounced surface topography. Thin Solid Films. 1999 Jul;348(1-2):227-232. doi: 10.1016/s0040-6090(99)00130-3. PubMed PMID: WOS:000081019700036:
- 57. Ramarotafika H, Lemperiere G. Influence of a d.c. substrate bias on the resistivity, composition, crystallite size and microstrain of WTi and WTi-N films. Thin Solid Films. 1995 Oct;266(2):267-273. doi: 10.1016/0040-6090(96)80032-0. PubMed PMID: WOS:A1995TK28500035;
- 58. Rogers BR, Tracy CJ, Cale TS. Compositional variation in sputtered Ti–W films due to re-emission Journal of Vacuum Science & Technology B. 1994 Sep-Oct;12(5):2980-2984. doi: 10.1116/1.587546. PubMed PMID: WOS:A1994PM72400018;
- 59. Rogers BR, Cale TS, Chang YK. Simulation and experimental study of re-emission during sputter deposition of Ti-W films. Journal of Vacuum Science & Technology a-Vacuum Surfaces and Films. 1996 May-Jun;14(3):1142-1146. doi: 10.1116/1.580284. PubMed PMID: WOS:A1996UR13400090;
- 60. Bergstrom DB, Tian F, Petrov I, et al. Origin of compositional variations in sputter-deposited Ti_xW_{1-x} diffusion barrier layers Appl Phys Lett. 1995 Nov;67(21):3102-3104. doi: 10.1063/1.114878. PubMed PMID: WOS:A1995TF57400017;
- 61. Rossnagel SM, Yang I, Cuomo JJ. Compositional changes during magnetron sputtering of alloys. Thin Solid Films. 1991 Apr;199(1):59-69. doi: 10.1016/0040-6090(91)90052-y. PubMed PMID: WOS:A1991FG71500008;
- 62. Dirks AG, Wolters RAM, Nellissen AJM. On the microstructure-property relationship of WTi (N) diffusion barriers. Thin Solid Films. 1990 Dec;193(1-2):201-210. doi: 10.1016/s0040-6090(05)80028-8. PubMed PMID: WOS:A1990EQ38300026;
- 63. Willer J, Pompl S, Ristow D. Sputter-deposited WB_x films. Thin Solid Films. 1990;188(1):157-163. doi: 10.1016/0040-6090(90)90201-n. PubMed PMID: WOS:A1990DQ31500015;
- 64. Simao RA, Costa AK, Achete CA, et al. Magnetron sputtering SiC films investigated by AFM. Thin Solid Films. 2000 Dec;377:490-494. doi: 10.1016/s0040-6090(00)01371-7. PubMed PMID: WOS:000166024600083;
- 65. Murakami Y, Shingyoji T. Compositional difference between films and targets in sputtering of refractory metal silicides. Journal of Vacuum Science & Technology a-Vacuum Surfaces and Films. 1990 Mar-Apr;8(2):851-854. doi: 10.1116/1.576929. PubMed PMID: WOS:A1990CU88900017;
- 66. Yamazaki T, Ikeda N, Tawara H, et al. Investigation of composition uniformity of MoSi_x sputtering films based on measurement of angular distribution of sputtered atoms. Thin Solid Films. 1993 Nov;235(1-2):71-75. doi: 10.1016/0040-6090(93)90245-k. PubMed PMID: WOS:A1993MG45700017;
- 67. Liao MY, Gotoh Y, Tsuji H, et al. Deposition of vanadium carbide thin films using compound target sputtering and their field emission. Journal of Vacuum Science & Technology A. 2005 Sep-Oct;23(5):1379-1383. doi: 10.1116/1.2008273. PubMed PMID: WOS:000232130400018;
- 68. Liao MY, Gotoh Y, Tsuji H, et al. Compound-target sputtering for niobium carbide thin-film deposition. Journal of Vacuum Science & Technology B. 2004 Sep-

- Oct;22(5):L24-L27. doi: 10.1116/1.1800491. PubMed PMID: WOS:000225048300003:
- 69. Walter C, Martinez C, El-Raghy T, et al. Towards large area MAX phase coatings on steel. Steel Research International. 2005 Feb-Mar;76(2-3):225-228. PubMed PMID: WOS:000227238700025;
- 70. Palmquist J-P, Jansson U, Seppanen T, et al. Magnetron sputtered epitaxial single-phase Ti 3 SiC 2 thin films. Appl Phys Lett. 2002;81(5):835-837.
- 71. Eklund P, Beckers M, Frodelius J, et al. Magnetron sputtering of Ti3SiC2 thin films,from a compound target. Journal of Vacuum Science & Technology A. 2007 Sep-Oct;25(5):1381-1388. doi: 10.1116/1.2757178. PubMed PMID: WOS:000249664400008;
- 72. Van Aeken K, Mahieu S, Depla D. The metal flux from a rotating cylindrical magnetron: a Monte Carlo simulation. Journal of Physics D-Applied Physics. 2008 Oct 21;41(20). doi: 10.1088/0022-3727/41/20/205307. PubMed PMID: WOS:000260131700048;
- 73. Möller W, Eckstein W, Biersack JP. TRIDYN-binary collision simulation of atomic collisions and dynamic composition changes in solids. Computer Physics Communications. 1988 Nov;51(3):355-368. doi: 10.1016/0010-4655(88)90148-8. PubMed PMID: WOS:A1988R544200008;
- 74. Möller W, Possel P. TRIDYN Users Manual. TRIDYN Users Manual. 2001.
- 75. MW Chase J, Davies C, JR Downey J, et al. JANAF Thermochemical Tables. Vol. 14. 1985. (J. Phys. Chem. Ref. Data; Suppl 1).
- 76. Kresse G, Hafner J. Ab initio molecular dynamics for open-shell transition metals. Phys Rev B. 1993;48(17):13115.
- 77. Kresse G, Hafner J. Ab initio molecular-dynamics simulation of the liquid-metal—amorphous-semiconductor transition in germanium. Phys Rev B. 1994;49(20):14251.
- 78. Perdew JP, Burke K, Ernzerhof M. Generalized gradient approximation made simple. Phys Rev Lett. 1996;77(18):3865.
- 79. Kresse G, Joubert D. From ultrasoft pseudopotentials to the projector augmentedwave method. Phys Rev B. 1999;59(3):1758.
- 80. Blöchl PE. Projector augmented-wave method. Phys Rev B. 1994;50(24):17953.
- 81. Monkhorst HJ, Pack JD. Special points for Brillouin-zone integrations. Phys Rev B. 1976;13(12):5188.
- 82. McDaniel EW. Collision phenomena in ionized gases. 1964.
- 83. Bayoumi AE, Bailey JA. Comparison of the wear resistance of selected steels and cemented carbide cutting tool materials in machining wood. Wear. 1985;105(2):131-144.
- 84. Sheikh-Ahmad J, Bailey J. The wear characteristics of some cemented tungsten carbides in machining particleboard. Wear. 1999;225:256-266.
- 85. Buršík J, Buršíková V, Souček P, et al. Nanostructured Mo-BC coatings. Romanian Reports in Physics. 2016;68(3):1069-1075.
- 86. Buršíková V, Sobota J, Grossman J, et al. Study of Fracture Resistance of Nanolaminate Coatings Using Indentation and Impact Tests. Solid State Phenomena. 2017;258:318-321.
- 87. Gleich S, Breitbach B, Peter NJ, et al. Thermal stability of nanocomposite Mo2BC hard coatings deposited by magnetron sputtering. Surf Coat Tech. 2018.

- 88. Zábranský L, Buršíková V, Souček P, et al. Thermal stability of hard nanocomposite Mo-BC coatings. Vacuum. 2017;138:199-204.
- 89. Bolvardi H, Music D, Schneider JM. Interaction of Al with O2 exposed Mo2BC. Applied Surface Science. 2015;332:699-703.
- 90. Gulbransen E, Andrew K, Brassart F. Oxidation of Molybdenum 550 to 1700 C. J Electrochem Soc. 1963;110(9):952-959.
- 91. Opeka MM, Talmy IG, Wuchina EJ, et al. Mechanical, thermal, and oxidation properties of refractory hafnium and zirconium compounds. Journal of the European Ceramic Society. 1999;19(13):2405-2414.
- 92. Zhang Z, Lim SH, Lai DMY, et al. Probing the oxidation behavior of Ti₂AlC MAX phase powders between 200 and 1000° C. Journal of the European Ceramic Society. 2017;37(1):43-51.
- 93. Zhang Y, Whitlow HJ, Winzell T, et al. Detection efficiency of time-of-flight energy elastic recoil detection analysis systems. Nuclear Instruments and Methods in Physics Research Section B: Beam Interactions with Materials and Atoms. 1999;149(4):477-489.
- 94. Arvizu MA, Wen R-T, Primetzhofer D, et al. Galvanostatic ion detrapping rejuvenates oxide thin films. ACS applied materials & interfaces. 2015;7(48):26387-26390.
- 95. to Baben M, Hans M, Primetzhofer D, et al. Unprecedented thermal stability of inherently metastable titanium aluminum nitride by point defect engineering. Mater Res Lett. 2017;5(3):158-169.
- 96. Pilling N. The oxidation of metals at high temperature. J Inst Met. 1923;29:529-582.
- 97. Ropital F, Chauvin Y. Corrosion and degradation of metallic materials: understanding of the phenomena and applications in petroleum and process industries. Editions technip; 2010.
- 98. Mo₂BC Crystal Structure: Datasheet from "PAULING FILE Multinaries Edition 2012" in SpringerMaterials (https://materials.springer.com/isp/crystallographic/docs/sd-0303158). Springer-Verlag Berlin Heidelberg & Material Phases Data System (MPDS), Switzerland & National Institute for Materials Science (NIMS), Japan.
- 99. Shi O, Xu L, Jiang A, et al. Synthesis and oxidation resistance of MoAlB single crystals. Ceramics International. 2019;45(2):2446-2450.
- 100. Gebhardt T, Music D, Takahashi T, et al. Combinatorial thin film materials science: From alloy discovery and optimization to alloy design. Thin Solid Films. 2012;520(17):5491-5499.
- 101. Herrig F, Music D, Völker B, et al. Ab Initio Guided Low Temperature Synthesis Strategy for Smooth Face—Centred Cubic FeMn Thin Films. Metals. 2018;8(6):384.
- 102. Gleich S, Soler R, Fager H, et al. Modifying the nanostructure and the mechanical properties of Mo2BC hard coatings: Influence of substrate temperature during magnetron sputtering. Mater Design. 2018;142:203-211.
- 103. Zhang S, Scheu C. Evaluation of EELS spectrum imaging data by spectral components and factors from multivariate analysis. Microscopy. 2017;67(suppl_1):i133-i141.
- 104. Hohenberg P, Kohn W. Inhomogeneous electron gas. Phys Rev. 1964;136(3B):B864.

- 105. Schneider JM, Anders A, Hjörvarsson B, et al. Hydrogen uptake in alumina thin films synthesized from an aluminum plasma stream in an oxygen ambient. Appl Phys Lett. 1999;74(2):200-202.
- 106. Greczynski G, Mráz S, Hultman L, et al. Venting temperature determines surface chemistry of magnetron sputtered TiN films. Appl Phys Lett. 2016;108(4):041603.
- 107. Walter C, Sigumonrong D, El-Raghy T, et al. Towards large area deposition of Cr2AlC on steel. Thin Solid Films. 2006;515(2):389-393.
- 108. Paier J, Marsman M, Hummer K, et al. Screened hybrid density functionals applied to solids. J Chem Phys. 2006;124(15):154709.
- 109. Bai Y, Qi X, Duff A, et al. Density functional theory insights into ternary layered boride MoAlB. Acta Mater. 2017;132:69e81.
- 110. Kota S, Agne M, Zapata-Solvas E, et al. Elastic properties, thermal stability, and thermodynamic parameters of MoAlB. Phys Rev B. 2017;95(14):144108.
- 111. Ade M, Hillebrecht H. Ternary borides Cr₂AlB₂, Cr₃AlB₄, and Cr₄AlB₆: the first members of the series (CrB₂)_nCrAl with n= 1, 2, 3 and a unifying concept for ternary borides as MAB-phases. Inorganic Chemistry. 2015;54(13):6122-6135.
- 112. Wang A, Shang S, Du Y, et al. Structural and elastic properties of cubic and hexagonal TiN and AlN from first-principles calculations. Comp Mater Sci. 2010;48(3):705-709.
- 113. Gibson JSK-L, Rezaei S, Rueß H, et al. From quantum to continuum mechanics: studying the fracture toughness of transition metal nitrides and oxynitrides. Mater Res Lett. 2018;6(2):142-151.
- 114. Tasnádi F, Odén M, Abrikosov IA. Ab initio elastic tensor of cubic Ti_{0.5}Al_{0.5}N alloys: dependence of elastic constants on size and shape of the supercell model and their convergence. Phys Rev B. 2012;85(14):144112.
- 115. Sansonetti JE, Martin WC. Handbook of basic atomic spectroscopic data. Journal of Physical and Chemical Reference Data. 2005;34(4):1559-2259.
- 116. Saloman EB. Energy levels and observed spectral lines of krypton, Kr I through Kr XXXVI. Journal of physical and chemical reference data. 2007;36(1):215-386.
- 117. Shang L, Gokuldoss PK, Sandlöbes S, et al. Effect of Si additions on the Al₂O₃ grain refinement upon oxidation of Cr₂AlC MAX phase. Journal of the European Ceramic Society. 2017;37(4):1339-1347.